Draft version April 6, 2016
Preprint typeset using LaTeX style emulateapj v. 5/2/11

arXiv:1604.01226v1 [astro-ph.HE] 5 Apr 2016

ON THE NATURE OF HYDROGEN-RICH SUPERLUMINOUS SUPERNOVAE

C. Inserra[1], S. J. Smartt[1], E. E. E. Gall[1,2], G. Leloudas[3,4], T.-W. Chen[5], S. Schulze[6,7], A. Jerkstarnd[1], M. Nicholl[8], J. P. Anderson[9], I. Arcavi[10,11], S. Benetti[12], R. A. Cartier[13], M. Childress[13], M. Della Valle[14], H. Flewelling[15], M. Fraser[16], A. Gal-Yam[3], C. P. Gutiérrez[17,18,19], G. Hosseinzadeh[10,20], D. A. Howell[10,20], M. Huber[15], E. Kankare[1], E. A. Magnier[15], K. Maguire[1], C. McCully[10,20], S. Prajs[13], N. Primak[15], R. Scalzo[21,22], B. P. Schmidt[23], K. W. Smith[1], B. E. Tucker[21,22], S. Valenti[24], M. Wilman[15], D. R. Young[1], and F. Yuan[21,22]

Draft version April 6, 2016

ABSTRACT

We present observational data for two hydrogen-rich superluminous supernovae (SLSNe), namely SN 2013hx and PS15br. These objects, together with SN 2008es are the only SLSNe showing a distinct, broad Hα feature during the photospheric phase and also do not show any clear sign of interaction between fast moving ejecta and circumstellar shells in their early spectra. Therefore we classify them as SLSN II (with no narrow lines in the photospheric spectra) as distinct from the known class of SLSN IIn (commonly used when narrow lines indicate circumstellar interaction). The lack of narrow lines suggests that their exceptionally high peak luminosity is not obviously powered by interaction and conversion of kinetic energy to radiative energy. Both transients show a slow decline at later times, and monitoring of SN2013hx out to 300 days after explosion indicates that the luminosity in this later phase does have a contribution from interaction. We detect strong, multi-component Hα emission at 240 days past maximum which we interpret as an indication of interaction of the ejecta with an asymmetric, clumpy circumstellar material. The spectra and photometric evolution of the two objects are similar to some bright type II (or type IIL) supernovae, although they have much higher luminosity and evolve on slower timescales. This comparison is qualitatively similar to how SLSN Ic compare with normal Ic in that the former are brighter and evolve more slowly. We find a significant broadband polarisation signal for PS15br, but uncertainties in the interstellar polarisation value means we cannot provide conclusive evidence for the source of the polarization. We applied two semi-analytical codes to fit the light curves of our two objects and SN 2008es. These are based on a diffusion model with energy input from a spinning down magnetar and the interaction between the ejecta and a dense uniform shell of H-rich material. Both scenarios can produce quantitative fits to the lightcurves but they both have weaknesses. The overall observational data set would tend to favour the magnetar, or central engine, model as the source of the peak luminosity although the clear signature of interaction shown at 240 days past maximum indicates that interaction can play a role in the luminosity evolution of superluminous type II SNe at some phases.

Subject headings: supernovae: general - supernovae: individual (SN 2013hx, PS15br, SN 2008es) - supernovae: interactions - stars: magnetars

[1] Astrophysics Research Centre, School of Mathematics and Physics, Queens University Belfast, Belfast BT7 1NN, UK; c.inserra@qub.ac.uk
[2] Max-Planck-Institut für Astrophysik, Karl-Schwarzschild-Str. 1, DE-85748 Garching-bei-München, Germany
[3] Department of Particle Physics and Astrophysics, Weizmann Institute of Science, Rehovot 7610001, Israel
[4] Dark Cosmology Centre, Niels Bohr Institute, University of Copenhagen, Juliane Maries vej 30, 2100 Copenhagen, Denmark
[5] Max-Planck-Institut für Extraterrestrische Physik, Giessenbachstraße 1, 85748, Garching, Germany
[6] Instituto de Astrofísica, Facultad de Física, Pontificia Universidad Católica de Chile, Vicuña Mackenna 4860, 7820436 Macul, Santiago, Chile
[7] Millennium Institute of Astrophysics, Vicuña Mackenna 4860, 7820436 Macul, Santiago, Chile
[8] Harvard-Smithsonian Center for Astrophysics, 60 Garden Street, Cambridge, Massachusetts 02138, USA
[9] European Southern Observatory, Alonso de Crdova 3107, Casilla 19, Santiago, Chile
[10] Las Cumbres Observatory Global Telescope Network, 6740 Cortona Dr., Suite 102 Goleta, Ca 93117
[11] Kavli Institute for Theoretical Physics, University of California, Santa Barbara, CA 93106, USA
[12] INAF, Osservatorio Astronomico di Padova, vicolo dell'Osservatorio 5, 35122, Padova, Italy
[13] Department of Physics & Astronomy, University of Southampton, Southampton, Hampshire, SO17 1BJ, UK
[14] INAFOsservatorio Astronomico di Capodimonte, Salita Moiariello 16, I-80131 Napoli, Italy
[15] Institute for Astronomy, University of Hawaii at Manoa,Honolulu, HI 96822, USA
[16] Institute of Astronomy, University of Cambridge, Madingley Road, Cambridge CB3 0HA, UK
[17] Millennium Institute of Astrophysics, Casilla 36-D, Santiago, Chile
[18] Departamento de Astronoma, Universidad de Chile, Casilla 36-D, Santiago, Chile
[19] European Southern Observatory, Alonso de Crdova 3107, Casilla 19, Santiago, Chile
[20] Department of Physics, University of California, Santa Barbara, CA 93106-9530, USA
[21] Research School of Astronomy and Astrophysics, Australian National University, Canberra, ACT 2611, Australia
[22] ARC Centre of Excellence for All-Sky Astrophysics (CAASTRO), The Australian National University, Canberra, ACT 2611, Australia
[23] Australian National University, Canberra, ACT 2611, Australia
[24] Department of Physics, University of California, Davis, CA 95616, USA

1. INTRODUCTION

Over the past few years, the current generation of wide-field optical surveys have discovered a new class of intrinsically bright transients. They show absolute magnitudes at maximum light of $M_{\rm AB} < -21$ mag, total radiated energies of order 10^{51} erg (e.g. see the early papers by Smith et al. 2007; Gezari et al. 2009; Pastorello et al. 2010; Quimby et al. 2011; Chomiuk et al. 2011; Inserra et al. 2013b) and now go by the common name of superluminous supernovae (Gal-Yam 2012). They are factors of 5 to 100 brighter than type Ia or normal core-collapse supernovae.

Two distinct groups have emerged so far. The first, and best studied, includes hydrogen-free SNe which have spectra at maximum light showing a blue continuum and a distinctive "W"-shaped spectra feature in absorption at ~ 4200 Å. The absorption has been identified as O II and these SNe have been labelled SLSNe I (Quimby et al. 2011; Gal-Yam 2012). Their spectra at about 30 days after peak are very similar to normal or broad-lined type Ic SNe at peak luminosity (Pastorello et al. 2010), and hence are also called SLSNe Ic (Inserra et al. 2013b). However, this broad group show two different types of light curve behaviour and they have been further divided in two subgroups of slow evolving - of which the prototype is SN 2007bi (Gal-Yam et al. 2009) - and fast evolving - of which the first example is SN 2005ap (Quimby et al. 2007, 2011). Although their physical nature remains debated, a plausible scenario is that of an explosion driven by a central engine, which deposits energy into the supernova ejecta and significantly enhances the luminosity (Woosley 2010; Kasen & Bildsten 2010; Dessart et al. 2012). The favoured central engine in this case is a magnetar which spins down due to magnetic dipole radiation, although accretion onto a central black hole is still a viable powering mechanism (Dexter & Kasen 2013). Inserra et al. (2013b) showed that quantitative fits with the magnetar model to a sample of low redshift SLSNe Ic reproduced the observed light curve and velocities quite well. Nicholl et al. (2015a) have assembled the largest sample to date - using all the literature data - suggesting that the fast and slow types could have the same powering mechanisms (central engine) with a range in ejecta masses being the dominant factor explaining the diversity. Regardless of the physical cause, SLSNe I are emerging as a new class of distance indicator. By analogy to SNe Ia, empirical relations can be used to standardise their magnitudes with a low scatter of $0.2 - 0.3$ mag as recently proposed by Inserra & Smartt (2014).

The second group is that of hydrogen-rich SNe. This includes the very bright, strongly interacting SNe such as SN 2006gy (Smith et al. 2007; Smith & McCray 2007; Ofek et al. 2007; Agnoletto et al. 2009) - of which the enormous luminosity is undeniably powered by the interaction of supernova ejecta with dense circumstellar (CSM) shells and, following the standard taxonomy, should be labeled SLSNe IIn (due to clear hydrogen narrow lines exhibited in the spectra). However there is also one known SLSN which in many ways is similar to the type Ic SLSNe, but with a distinct and broad Hα feature. This is SN 2008es, which was studied by Miller et al. (2009) and Gezari et al. (2009) and does not obviously show any signs of interaction between fast and slow moving ejecta and CSM shells. Another object, which goes by the name of CSS121015:004244+132827 shows weak but distinct and multi-component H emission (Benetti et al. 2014). This most likely appears to arise due to some form of interaction, but whether or not the same physics causes the similar extreme luminosity in CSS121015:004244+132827 and SN 2008es remains to be seen. It is plausible that there are multiple powering sources in any of these explosions. For example a central engine may power the bulk of the luminosity, but then interaction between the magnetar powered ejecta and some CSM shells (of varying density) could provide additional energy output and alter the spectra morphology. The object iPTF13ehe shows signs of interaction with a pre-existing H-rich shell (Yan et al. 2015), and this has been interpreted either as evidence for interaction powered luminosity (Yan et al. 2015), consequence of a binary system (Moriya et al. 2015) or a combination of power sources (Wang et al. 2015). Hereafter we will refer to events without obvious spectral signatures of interaction as SLSNe II whereas those with narrow spectral features and obviously powered by interaction will be referred to as SLSNe IIn. It appears that SLSN which show hydrogen are rarer than those without hydrogen. It is certainly true that they are less well studied. More of them are required to investigate the link between the SLSN II and the better quantified SLSN I or Ic sample. In this paper we present two more SLSN II objects, followed in detail by the Public ESO Spectroscopic Survey for Transient Objects (PESSTO; Smartt et al. 2015) with $\rm H_0 = 72\ km\,s^{-1}$, $\Omega_{\rm M} = 0.27$, $\Omega_{\lambda} = 0.73$ adopted as standard cosmology.

The main focus of the paper - the study of two H-rich objects - is presented in Sections 2 & 3 and analysed in Sections 4, 5, 6 & 7. Finally, a discussion about the origin of these H-rich transients is presented in Section 8, followed by a short summary in Section 9.

2. DISCOVERY

2.1. *SN 2013hx*

SN 2013hx (SMTJ013533283-5757506) was discovered by the SkyMapper Transient (SMT) and Supernova Survey (Keller et al. 2007; Scalzo et al. 2013) on the 27th December 2013 in g and r bands. Three weeks before the discovery, on MJD 56632.55, a SMT image shows no detection of the transient to $r \simeq 20.28$ mag. Hence we can determine the epoch of explosion to around twenty days, at least as far as the sensitivity of the images allow. The object coordinates have been measured on our astrometrically calibrated images: $\alpha = 01^{\rm h}35^{\rm m}32^{\rm s}.83 \pm 0^{\rm s}.05$, $\delta = -57^{\rm o}57'50.6" \pm 0".05$ (J2000). The object brightened slowly by ~ 1 mag in the observed g-band from discovery to peak and the photometry is given in Appendix B, Table 6. It was classified by the Public ESO Spectroscopic Survey of Transient Objects (PESSTO, Smartt et al. 2015) as a superluminous supernova similar to SN 2010gx (Pastorello et al. 2010) and CSS121015:004244+132827 (Benetti et al. 2014) on February 20 UT (Campbell et al. 2014; Scalzo et al. 2014). The spectrum showed a blue continuum with broad features in the blue together with a narrow emission feature at $\sim$7500 Å consistent with Hα setting the object at $z = 0.125$, equivalent to

a luminosity distance of $d_{\rm L} = 570.3$ Mpc. The Galactic reddening toward the position of the SN is E(B-V)=0.02 mag (Schlafly & Finkbeiner 2011).

Deep *gri* images taken by PESSTO with the New technology telescope (NTT)+EFOSC2 on the 10th of December 2015 find an extended, faint source at , $\alpha = 01^{\rm h}35^{\rm m}32^{\rm s}.78 \pm 0^{\rm s}.05$, $\delta = -57^{\rm o}57'52.3" \pm 0".05$ (J2000) which is at $2''$ from SN location (4.36 kpc at $z = 0.125$). The magnitudes of this likely host galaxy are $g = 24.43 \pm 0.16$, $r = 23.20 \pm 0.16$ and $i = 21.82 \pm 0.16$. This source was not detected in the NIR with deep JHK images taken by PESSTO with the NTT+SOFI on the 17 December 2015 ($J > 23.1$, see Table 6 for the limits in each filter). Even deeper images from Magellan+IMACS on the 1 February 2016 showed faint flux closer to the location of SN 2013hx (within $0\farcs5$) at magnitude $g = 24.71 \pm 0.38$, $r = 24.55 \pm 0.35$ and $i = 23.54 \pm 0.32$. This flux could either be the true host or residual flux from SN 2013hx or a combination of both. Given that the Magellan detections are close to 3σ significance and that star/galaxy separation is not reliable at these flux limits, we assume that the host of SN 2013hx is the brighter, clearly resolved galaxy $2''$ from the transient. We call this Host A in Table 6 and call the marginally detected fainter source Host B (more details on the Magellan data will be presented in Schulze et al., in prep).

2.2. *PS15br*

PS15br was discovered by the Pan-STARRS Survey for Transients (PSST, Huber et al. 2015)[25] on 16 February 2015 at $w_{\rm P1} = 19.10 \pm 0.02$, confirmed as a transient source the day after and subsequently detected by the Catalina Real-time Transient Survey (CRTS, Drake et al. 2009, with IDs CSS150226-112519+081418 and MLS150612-112519+081418) at $R = 18.3$ mag on 26 February 2015. The closest pre-detection image is on the 16 January 2015 from CRTS images. We measured the objects coordinates on our astometrically calibrated images: $\alpha = 11^{\rm h}25^{\rm m}19^{\rm s}.22 \pm 0^{\rm s}.05$, $\delta = 8^{\rm o}14'18.9" \pm 0".05$ (J2000). The SN was observed to rise slowly with these multiple detections by PSST and CRTS and was then classified by PESSTO on the 11th of March 2015 (Fraser et al. 2015) as a superluminous supernova at $z = 0.101$, corresponding to a luminosity distance of $d_{\rm L} = 456$ Mpc. The foreground reddening is E(B-V)=0.06 mag from Schlafly & Finkbeiner (2011).

We retrieved stacks from the Pan-STARRS1 Science Consortium 3π survey (Tonry et al. 2012; Schlafly et al. 2012; Magnier et al. 2013) with total exposure times of g (720s), r (590s), i (1800s), z (930s) from before the explosion of PS15br and which are unlikely to contain SN flux. Aperture photometry produced the following AB magnitudes for the extended host galaxy $g_{\rm P1} = 22.39 \pm 0.11$, $r_{\rm P1} = 22.18 \pm 0.12$, $i_{\rm P1} = 21.70 \pm 0.09$, $z_{\rm P1} = 22.15 \pm 0.11$ mag. We estimate the centre of this dwarf host galaxy ($M_g = -16.1$) is $0.6''$ from SN location (which would be 1 kpc at $z = 0.101$) and within the uncertainties is effectively coincident. The photometric measurements of the host are in agreement with the Sloan magnitudes of the galaxy SDSS J112519.21+081417.9 listed in the SDSS DR12 (Alam et al. 2015). We note that SDSS DR12 gives a photometric redshift estimate of $z_{\rm phot} = 0.752 \pm 0.14$, which is further illustration of the difficulty in using photometric estimates at low redshift to usefully constrain distances and luminosities of transients in an automated and reliable way (see discussion in Smartt et al. 2016).

[25] http://star.pst.qub.ac.uk/ps1threepi/psdb/

3. OBSERVATIONS AND DATA REDUCTION

Both objects were immediately selected by PESSTO as follow-up science targets and a combination of optical, near infrared (NIR) and ultraviolet (UV) photometric monitoring was carried out. The epochs of all the data, as well as the telescopes and instruments used are listed in Appendix B.

All images were reduced (trimmed, bias subtracted and flat-fielded) by the SMT, PSST, Las Cumbres Observatory Global Network (LCOGT, Brown et al. 2013), Liverpool Telescope (LT, Steele et al. 2004), CRTS and PESSTO pipelines. Photometric zero-points and colour terms were computed using observations of standard fields (UBVRI in Vega and *griz* in AB system). We then calibrated the magnitudes of local stellar sequences shown in Appendix C. The average magnitudes of the local-sequence stars were used to calibrate the photometric zero-points in non-photometric nights. The near-infrared JHK photometry was carried out on SOFI on the NTT and the data were again reduced as discussed in Smartt et al. (2015). Magnitudes were calibrated to the Two Micron All Sky Survey system using local sequence stars. The magnitudes of the SNe, obtained through a point spread function (PSF) fitting technique using standard procedures in IRAF[26], were measured on the final images. The uncertainties reported in the Appendix B Tables 6, 7 & 8 were estimated by combining in quadrature the errors of photometric calibration and those on the instrumental magnitudes. When the objects were xnot detected, limiting magnitudes were estimated by placing artificial stars of different magnitudes at the expected SN positions. When necessary - i.e. after 170d for SN 2013hx and 100d for PS15br - we applied a template subtraction technique (through the HOTPANTS[27] package based on the algorithm presented in Alard 2000). The instruments used to obtain the templates were NTT for SN 2013hx and PSST for PS15br. The same frames were used to measure the host magnitudes and host NIR limit magnitudes (see Sections 2.1 & 2.2).

Differences between passbands were taken into account applying a passband correction (P-correction) using the SuperNova Algorithm for P-correction (SNAP) in the S3 package (see Appendix A for further details). This P-correction is similar to the S-correction (Stritzinger et al. 2002; Pignata et al. 2004).

Ultraviolet ($uvw2, uvm2, uvw1$; see Poole et al. 2008) observations, obtained by UVOT on board of the *Swift* satellite (P.I. Margutti for SN 2013hx and Inserra for PS15br) were reduced using the HEASARC[28] software. We analysed these publicly available data independently.

[26] Image Reduction and Analysis Facility, distributed by the National Optical Astronomy Observatories, which are operated by the Association of Universities for Research in Astronomy, Inc, under contract to the National Science Foundation.

[27] http://www.astro.washington.edu/users/becker/hotpants.html

[28] NASA's High Energy Astrophysics Science Archive Research Center

TABLE 1
Main properties of the SLSNe II here presented.

	SN 2013hx	PS15br
Alternative names	SMTJ013533283-5757506	CSS150226-112519+081418 MLS150612-112519+081418
α (J2000.0)	$01^{h}35^{m}32^{s}.83$	$11^{h}25^{m}19^{s}.22$
δ (J2000.0)	$-57^{o}57'50.6$"	$8^{o}14'18.9$"
z	0.125	0.101
Peak g (mag)	-21.70	-20.22
E(B-V) (mag)	0.02	0.06
L_{ugriz} peak (x 10^{43} erg s^{-1})	10.78	2.43
Light curve peak (MJD)	56684.50 ± 1.00	57089.25 ± 2.00
Host r (mag)	-15.58(A),-14.81(B)	-16.25

Swift u, b, v aperture magnitudes were transformed to Johnson system by applying a shift after comparison with optical ground-based data taken close in time.

The journal of spectroscopic observations is listed in Table 12. The majority of the follow-up spectra where taken with PESSTO and the NTT. Integral field spectra were also taken with the ANU 2.3 m telescope + the Wide Field Spectrograph (WiFeS, Dopita et al. 2010) at Siding Spring Observatory in New South Wales, Australia. A final spectrum of PS15br was taken with the SuperNova Integral Field Spectrograph (SNIFS, Lantz et al. 2004) at the 2.2m University Hawaii Telescope. A series of spectra of SN 2013hx was taken with the VLT+FORS2[29] in the second season of observations, and combined together into one deep late-time spectrum. These FORS2 exposures had a total of 11×1230 sec and 1×1800 and were taken on the nights of 22-24 October 2014 through service mode on the VLT (giving an on-sky total exposure time of 4hr 15min 30sec). The NTT spectral data were reduced using the PESSTO pipeline (Smartt et al. 2015), while the VLT+FORS spectra were reduced in the REFLEX environment (Freudling et al. 2013) and the SNIFS spectrum using standard IRAF procedures as described in Smartt et al. (2016). Optimal extraction of the spectra was adopted to improve the final signal-to-noise (S/N) ratio. Wavelength calibration was performed using spectra of comparison lamps acquired with the same configurations as the SN observations. Atmospheric extinction correction was based on tabulated extinction coefficients for each telescope site. The WiFeS spectra were reduced with PYWIFES[30] package (Childress et al. 2014) to produce data cubes, from which the final spectra were obtained using a PSF weighted extraction routine. Flux calibration was performed using spectrophotometric standard stars observed on the same nights with the same set-up as the SNe. The flux calibration was checked by comparison with the photometry, integrating the spectral flux transmitted by standard *griz* filters and adjusted by a multiplicative factor when necessary. The resulting flux calibration is accurate to within 0.1–0.2 mag.

All reduced spectra (and calibrated NIR images), taken at the NTT before 2014 April 30, are available from the ESO Science Archive Facility as PESSTO SSDR2 and details of data access are provided on the PESSTO website[31]. Data taken after this date will form part of the next public release of public data products (due in 2016). All spectra will also be available through WISeREP[32] (Yaron & Gal-Yam 2012).

4. LIGHT CURVES

SN 2013hx shows a light curve with a 30 day rise in the observer frame in both g and r bands (see Fig. 1) with relatively close non-detections pointing toward to a rise time of ∼40 days (∼37d in rest-frame) from explosion. The decline after peak is observed only in V, g, and r bands. The rest-frame decline in g-band is 2.0 mag $100d^{-1}$ (phase<10d), while in V-band is 4.5 mag $100d^{-1}$ (phase>20d) suggesting a linear decline similar to that of SN 2008es showing 2.9 mag $100d^{-1}$ in g-band. This would imply SLSNe II fall on the right part of the $s2/M_{\rm max}$ distribution of type II SNe showed by Anderson et al. (2014a). The untimely end of our observational campaign in March 2013 was due to the right ascension of the object [33]. The second season started when it reappeared again in July and PESSTO restarted its annual observing periods in August 2013. Hence the follow-up campaign recovered SN 2013hx some five months after maximum light in this second season. From 160d onward the light curves show a steady decline in all bands. The decline is close to that of ^{56}Co decay, but our interpretation later in this paper suggests that it appears to the consequence of ongoing interaction with CSM material (see Section 7.2).

PS15br was detected during the rise phase, only in the w-band of PSST and by the Catalina Sky Survey (CSS). We continued to observe the SN until it disappeared behind the Sun in July 2015. The non-detection of the transient 30d before the first detection suggests a rise time of ∼35d in the rest-frame and hence similar to that of SN 2013hx. We fit the data with a low-order polynomial and find the peak epoch consistent with MJD 57089.25±2.00. PS15br shows a fairly rapid and linear decline in the UV and u bands after peak, which is gradually less steep in the redder bands. In B, V, g and r bands, the light curves show a slower second decline with 1.2 mag $100d^{-1}$ in g-band between 30-90 days post peak in rest-frame. Such light curves show an overall slower evolution than other objects at similar absolute magnitude (Arcavi et al. 2016). Curiously, last two epochs of

[29] Very Large Telescope + FOcal Reducer and low dispersion Spectrograph
[30] http://www.mso.anu.edu.au/pywifes/
[31] www.pessto.org
[32] http://wiserep.weizmann.ac.il/home
[33] Part of these data, following the procedures here described, were previously presented in Nicholl et al. (2015a).

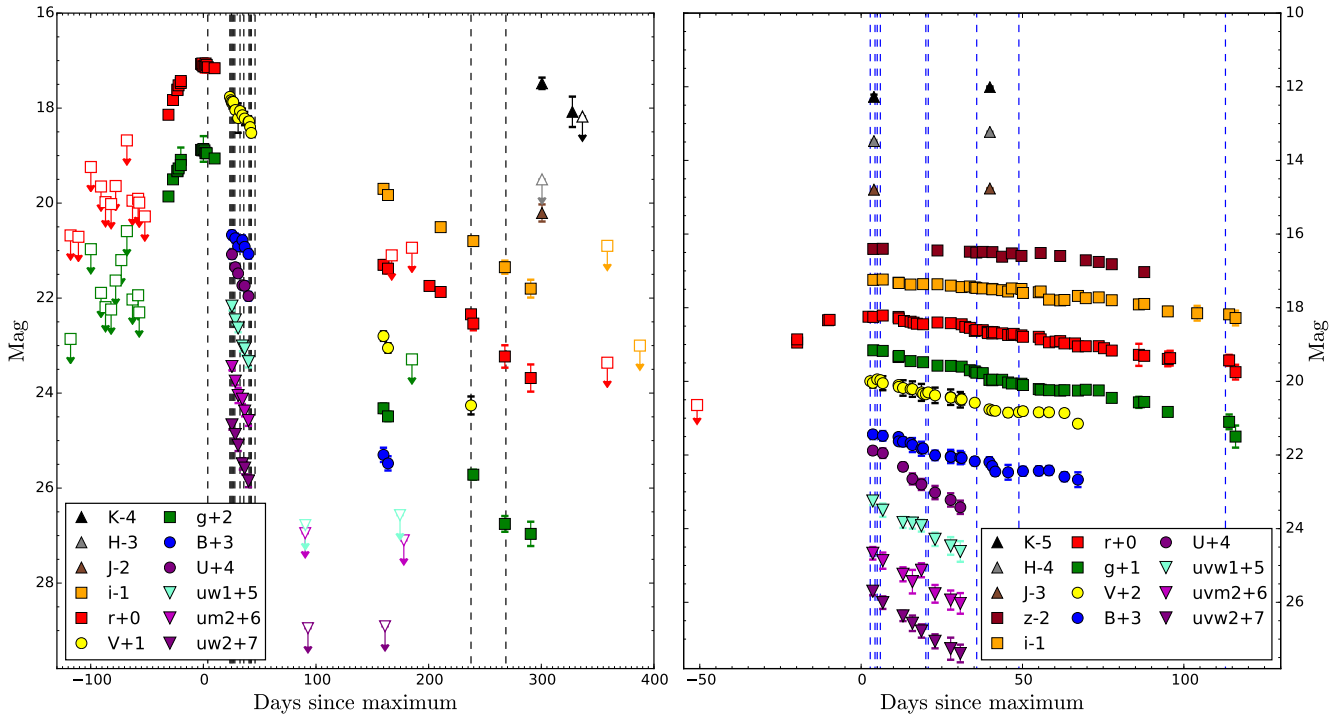

FIG. 1.— Left: $uvw2uvm2uvw1UBVgriJHK$ light curve evolution of SN 2013hx in the observed frame. Right: $uvw2uvm2uvw1UBVgrizJHK$ light curve evolution of PS15br in the observed frame. Open symbols denote limits. Phase is with respect to maximum light at observed frame in r-band. The epochs of SN 2013hx and PS15br spectra are marked with black and blue vertical dashed lines, respectively

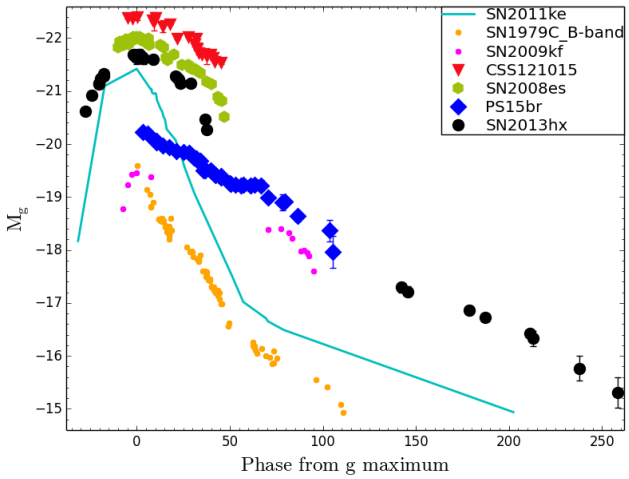

FIG. 2.— Comparison of restframe g-band light curve evolution of SN 2013hx and PS15br with those of the well sample SLSNe I 2011ke, the SLSN II 2008es, the interacting SLSN CSS121015, the bright type II (or type IIL) SNe 1979C and the bright type IIP SN 2009kf. Phase is with respect to g maximum light. Time dilation and K-correction, through SNAKE, have been applied to all SNe.

PS15br could suggest a faster decrease similar to what experienced by type IIP and some IIL at similar phase (see Valenti et al. 2015), which correspond to the end of the H recombination. However, only two epochs are not enough to draw any conclusion.

In Fig. 2 we compare the absolute magnitudes in g-band of our two objects together with that of the other SLSN II SN 2008es (Gezari et al. 2009; Miller et al. 2009), the SLSN CSS121015 (Benetti et al. 2014), the SLSN Ic 2011ke (Inserra et al. 2013b), the bight type II SN1979C (B-band, Barbon et al. 1982) and the bright type IIP SN 2009kf (Botticella et al. 2010). In calculating absolute magnitudes (and subsequently bolometric magnitudes), we have assumed negligible internal host galaxy reddening for all the objects, and applied only foreground reddening. No Na ID absorption features due to gas in the hosts were observed. However, we can not exclude possible dust extinction from the hosts, therefore the absolute magnitudes reported here are technically lower limits. We computed K-corrections for each SN using the spectral sequence we have gathered. For photometric epochs for which no spectra were available, we determined a spectral energy distribution (SED) using the multi-color photometric measurements available. This SED was then used as a spectrum template to compute the K-corrections. Comparisons between the two methods (K-correction directly from spectra, or with the photometric colours) showed no significant differences. All K-corrections have been obtained with the SuperNova Algorithm for K-correction Evaluation (SNAKE, presented in Appendix A).

The light curves of SN 2013hx and SN 2008es are notably similar. CSS121015 also exhibits a fairly similar decline over the first 40 days, but is 0.5 mag brighter. The only object with a well observed rise in the g-band is that of SN 2013hx, which appears to be slower than the typical type SLSN Ic events like SN 2011ke. PS15br is more than one magnitude fainter and sits in the gap between normal luminosity type II SNe and SLSNe II such as SNe 2008es and 2013hx. Although PS15br exhibits a similar decline to SN 2008es and SN 2013hx over the first 30 days, it clearly does not show the faster decline observed after this epoch - it remains on quite a linear

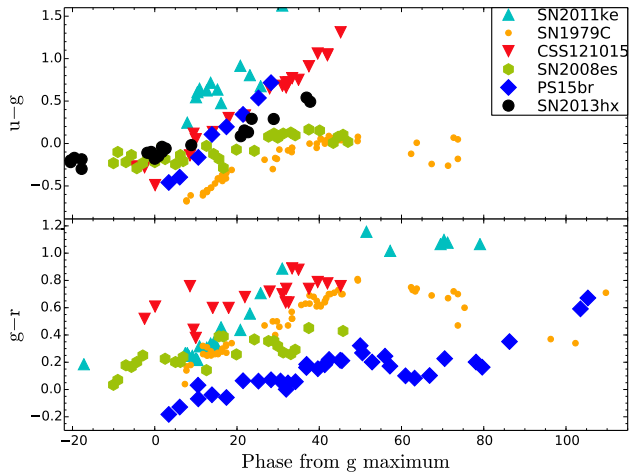

FIG. 3.— Comparison of the dereddened and K-corrected color evolutions. SN 2013hx and PS15br are shown together with the same SNe of Fig. 2, excluding SN 2009kf. SNe 1979C color curve is actually U-B (top panel) and B-V (bottom panel).

decline for nearly 100 days. It also shows a similar overall decline rate similar to that of SN 2009kf (Botticella et al. 2010).

4.1. *Color curves*

Since color curves are useful probes of the temperature evolution of the SNe, we computed the rest-frame curves, after accounting for the reddening and redshift effects of time-dilation and K-correction. In Fig. 3 SN 2013hx and SN 2008es show a constant u-g increase toward redder values. SN 2013hx appears to show a similar steady increase until 250d after maximum (in the restframe), although we caution that the obvious gap of 100 days precludes drawing a conclusion that the evolution was steady. However PS15br is significantly bluer than other SLSNe II at peak. Its color evolution is also steep, but and similar to SN 2011ke and CSS121015. We also note that after 20 days, the u-g color evolution gradient of SLSNe II is similar to that of bright type II (or type IIL). Although the former is shifted redwards overall.

The g-r colors show a similar behavior with a slow, monotonic increase toward redder colors. SLSN II do not show the constant color exhibited by SLSNe Ic from the pre-peak phase to ∼15d (Inserra et al. 2013b). In general the colors evolve more slowly to the red than type IIL SNe. It appears that PS15br g-r shows a turnover at at 50 days and evolves bluewards before turning to the red again. However, considering the scatter and compare this color curve with the temperature behavior (see Section 7.1) it may be a flattening in the color evolution (at g-r ∼0.24) rather than a blueward evolution. The object then clearly evolves to the red afterwards and with $g - r = 0.6$ after 100d it appears similar to SN 2013hx and type II SNe.

5. BOLOMETRIC LUMINOSITY

UV to NIR photometry at all epochs is required to obtain a direct measurement of the full bolometric luminosity. This is typically difficult to achieve at all epochs during a SN evolution. For PS15br we have only a few NIR points, and have good UV coverage during the first 30 days only. The later is not a major problem for the rest of the light curve if the colour evolution continues, as the UV contribution reduces significantly. Despite the lack of data, valid corrections can be applied to the observed photometric bands to compute the total bolometric flux.

The effective temperatures of the photospheres of SLSNe II during their first 30-50 days after explosion are between $T_{\rm bb} \sim 10000 - 16000$ K (see Section 7.1). This means that their fluxes peak in the UV ($\lambda < 3000$ Å) during this period while our rest-frame $ugri$ bands typically cover from 3500 Å redwards. Thus a significant fraction of the flux is not covered by the optical $ugri$ imaging, as testified by the UV to total luminosity ratio for SN 2008es and PS15br (see Fig. 4). At around 20d after peak, the effective temperatures tend to drop below 10000 K, hence the SEDs peak between 3000 Å and 4000 Å. Although the peak of the SED moves redward, a significant amount of the bolometric flux is radiated in the UV even during these late stages. In the following, we will use the term "pseudo-bolometric light curve" to refer to a bolometric light curve determined using only the optical filters with the flux set to zero outside the observed bands.

Initially, the broad band magnitudes in the available optical bands were converted into fluxes at the effective filter wavelengths, then were corrected for the adopted extinctions (cfr. Section 2). A SED was then computed over the wavelengths covered and the flux under the SED was integrated assuming there was zero flux beyond the integration limits. Fluxes were then converted to luminosities using the distances previously adopted. We initially determined the points on the pseudo-bolometric light curves at epochs when $ugri$ were available simultaneously (or very close in time) and later for epochs with coverage in less than the four filters. Magnitudes from the missing bands were generally estimated by interpolating the light curves using low-order polynomials between the nearest points in time. For some points this interpolation was not possible and hence we extrapolated the magnitudes assuming constant colors from neighbouring epochs.

Since SN 2013hx and SN 2008es have similar optical light curves (see Section 4) we built the SN 2013hx bolometric light curve considering the same NIR flux contribution of SN 2008es at early epochs. As a quality check of this procedure we estimated the bolometric light curve integrating SN 2013hx SED from UV to NIR wavelengths and found similar values to those of the previous method. We considered the difference between these two methods as errors in the evaluation of the SN 2013hx bolometric light curve. In Fig. 4 (right panel) we compared UV and NIR contributions to the total bolometric luminosity of SN 2013hx and PS15br with that of the SN 2008es. The UV contributions are similar and drop to zero after 60 days from maximum, while the NIR contribution increases with time. We have late NIR data in JHK information only for SN 2013hx, whereas SN 2008es only has data in the J and H bands at these epochs where the NIR contribution becomes significant. If we were to ignore the PS15br K-band contribution, the two percentages of NIR contribution are similar. Therefore when we evaluated the full bolometric light curves of SN 2013hx and SN 2008es we added the K-band contribution esti-

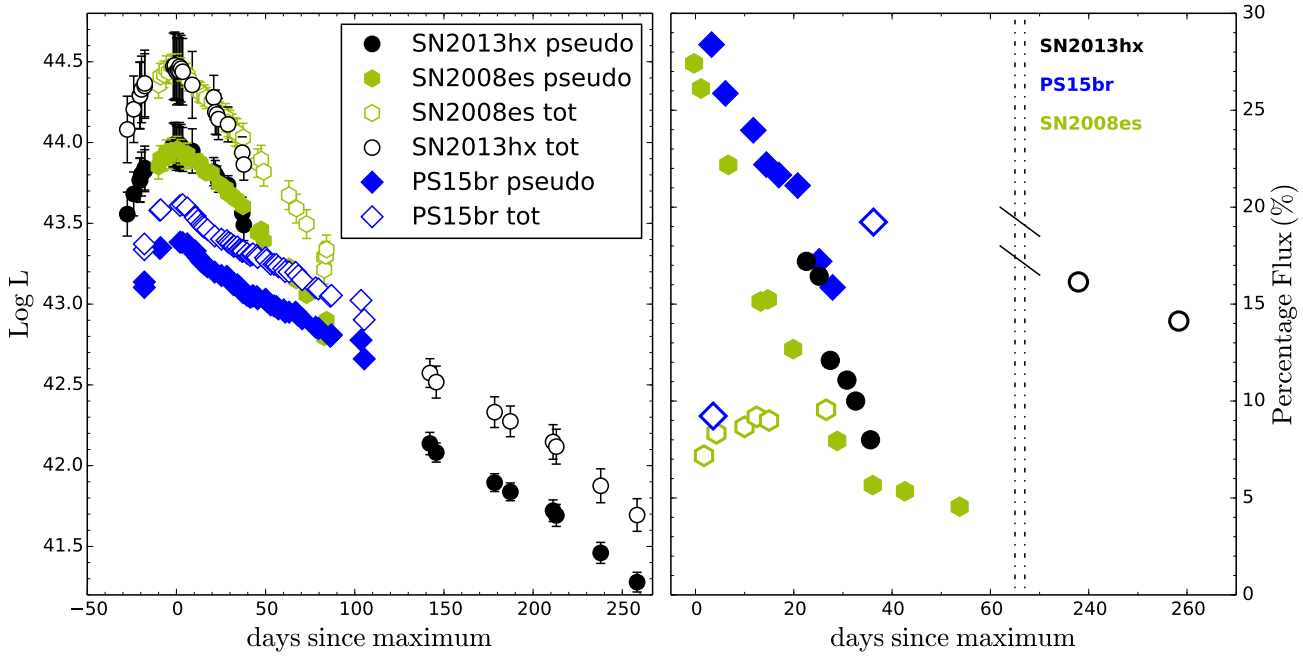

FIG. 4.— Left: pseudo (filled symbols) and proper bolometric (open symbols) of three SLSNe II. Right: percentage of the bolometric flux in UV (filled symbols) and NIR (open symbols) with respect to the total bolometric flux derived from data of SLSNe II.

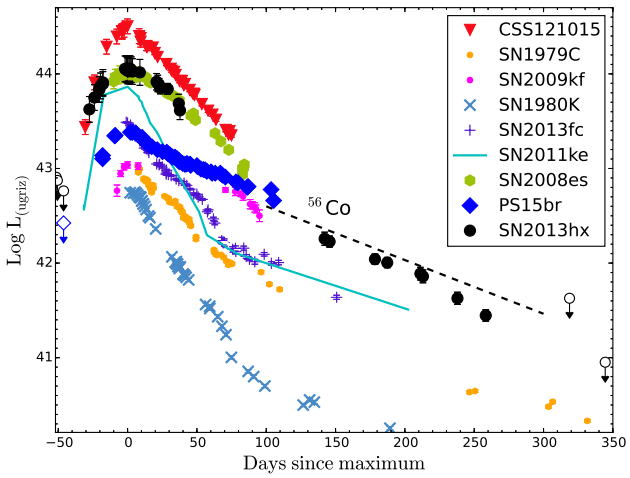

FIG. 5.— Comparison of pseudo bolometric light curves (*ugriz*) of SN 2013hx, PS15br and type Ic SLSNe 2011ke, type II SLSN 2008es, SLSN CSS121015, the bright type II (or type IIL) 1979C and 1980K and the bright, mild interacting type II 2013fc. These bolometric light curves are computed after correcting the observed broadband photometry for time dilation and applying *K*-corrections, through SNAKE, and extrapolating up to *z* band when this was unavailable. The dashed line is the slope of ^{56}Co to ^{56}Fe decay.

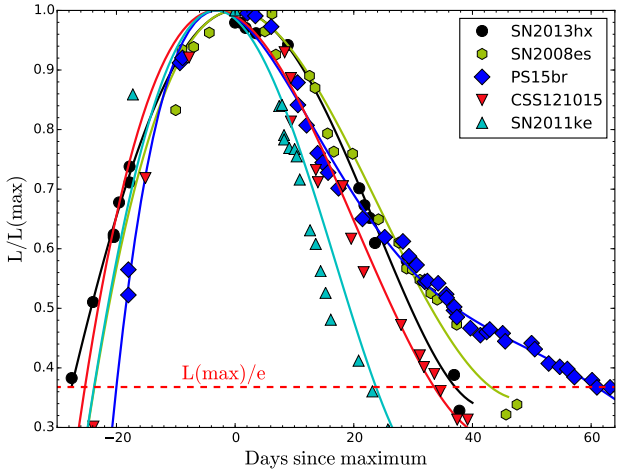

FIG. 6.— Pseudo bolometric light curves (*ugriz*) normalized to the maximum of the polynomial fit. The luminosity equivalent to L(max)/e is highlighted by a red dashed line.

mated specifically by PS15br NIR data.

The peak luminosities of our bolometric light curves are $L_{SN\ 2013hx} \approx 2.75\times10^{44}$ erg s^{-1}, $L_{PS15br} \approx 4.15\times10^{43}$ erg s^{-1} and $L_{SN\ 2008es} \approx 3.00\times10^{44}$ erg s^{-1}. While the maximum luminosities reached by the pseudo-bolometric light curves are almost factor two lower.

Fig. 5 compares the pseudo-bolometric light curves *ugriz* of our sample of SLSNe II - namely SN 2013hx, SN 2008es, PS15br - with that of CSS121015, a SLSN Ic (SN 2011ke) and hydrogen-rich core collapse SNe. We note that the extrapolation up to *z* band has been done assuming constant color from neighbouring epochs or integrating the best fit blackbody to the available SED up to the *z* band coverage.

The comparison between SN 2011ke pseudo-bolometric light curves shows that both SN 2013hx and SN 2008es have fairly similar shaped profiles within 10-20 days of peak. This requires *u*- (or alternatively U-) band data to make a meaningful comparison, due to the temperatures at these epochs. To make quantitative comparisons of the light curve widths, we measured a width when the pseudo-bolometric flux is $1/e$ less than that at maximum light in order to qualitatively match the estimates of τ_m in Nicholl et al. (2015b). When these epochs were not specifically covered by a data point, we used low order polynomial fits to interpolate and find a value (see Fig. 6). The values are reported in Table 2. We do note

TABLE 2
WIDTH OF SLSNE PSEUDO-BOLOMOTRIC *ugriz* LIGHT CURVES

SN	width (day)	rise (day)	decline (day)
SN 2013hx	64 ± 3	27	37
PS15br	80 ± 5	20	60
SN 2008es	67 ± 5	24	43
CSS121015	58 ± 3	25	33
SN 2011ke	48 ± 3	24	24

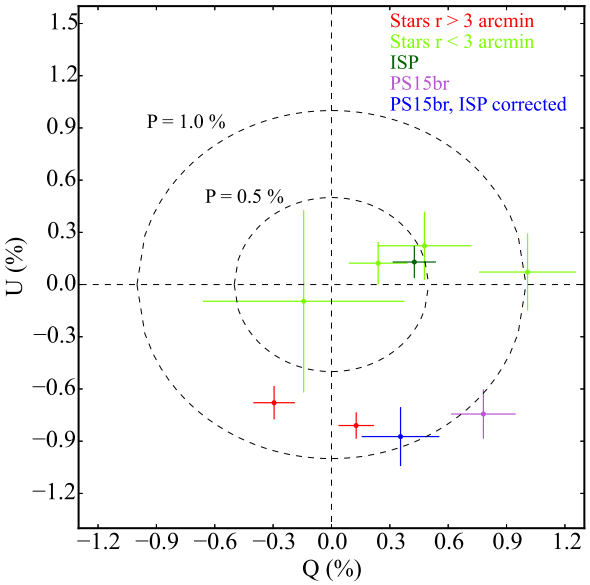

FIG. 7.— Q-U plane of PS15br at +6d from maximum light. Concentric circles show polarization degrees of 0.5% and 1.0%.

that such values are slightly different than those reported in Nicholl et al. (2015a).The errors reported are estimated from the differences between the values achieved with different polynomials orders and time baselines.

As highlighted before, the decline of SLSNe II tend to be slower than that of SLSNe Ic such as SN 2011ke, while the rise time is comparable for all the object. On the other hand, the $1/e$ width is around 70 for SLSNe II and around 50 for SLSNe Ic and CSS121015. For the latter, that is a consequence of the sharp rise and decline from peak luminosity. We also note as SN 2013hx, SN 2008es and CSS121015 have a similar decline from 20 to 50 days and also up to 70 days in the case of SN 2008es and CSS121015. This decline is similar to that of SNe 1979C and 1980K even if the similarity with the former is more striking. The width of the main peak in PS15br is also not comparable to that of the SLSN IIn 2006gy, as the latter has a much wider light curve of $\sim$110 days. Furthermore the PS15br peak is strongly asymmetric (see Fig. 5, Fig. 6 & Table 2) suggesting the light curve is probably now driven by interaction at least until 10 days after peak epoch. The slower decline experienced by PS15br is comparable to that of the bright type IIP SN 2009kf and could be the consequence of a more massive hydrogen layer - and hence higher contribution from hydrogen recombination - than those of SLSNe II. Alternatively it could be due to interaction in a similar manner to what has been observed in weakly interacting type II such as SN 2007pk (Inserra et al. 2013a) and PTF11iqb (Smith et al. 2015) or the bright SN 2013fc (Kangas et al. 2016), which is the brightest among them and reach a similar optical brightness of PS15br with, however, a faster decline. In these cases a weaker interaction than what we normally associate with SNe IIn has been invoked which affects the spectra and light curve evolution in a less dramatic way.

6. POLARIMETRY

On 2015 March 14 UT 05.2, corresponding to a rest-frame phase of 6 days after maximum, we obtained broadband polarimetry of PS15br with VLT/FORS2 using the V filter. We observed it in four different half-wave retarder plate angles: 0, 22.5, 45 and 67.5 deg. The exposure time was 150 s for each angle. The data were reduced in a standard manner by using bias and flat frames, without polarisation units in the light path. We obtained PSF photometry of PS15br and six field stars in the field of view (FOV) and determined their Stokes parameters. The measurements were corrected for instrumental polarisation (Patat & Romaniello 2006) and interstellar polarisation (ISP). For more details on the reductions and analysis, the reader is referred to Leloudas et al. (2015), where similar procedures were used.

Fig. 7, shows the location of PS15br and the field stars on the $Q-U$ plane, after correcting for instrumental polarisation. The error bars that are shown are the measurement errors resulting from the PSF fitting and essentially depend on the S/N ratio ($\sim$500 for PS15br). The field stars (light green and red points) present a significant scatter in this plane and the SN signal (purple) is comparable to the one of the field stars. It is therefore likely that the signal of the field stars and the SN is dominated by ISP. Patat & Romaniello (2006) showed that the instrumental-induced polarisation in FORS1 - an instrument with identical design to that of FORS2 - has a radial pattern with polarisation increasing as we move away from the optical axis. The two field stars that are the main cause of the scatter (red) are at the outskirts of the FOV, more than 3.6′ from PS15br, which is in the centre of the FOV. On the other hand, the measurement of the stars closer to the object (light-green) are self-consistent with each other and can be used for a more accurate determination of the ISP. The ISP is shown in Fig 7 as the weighted average of the light-green stars. Therefore, despite the fact that all points have been corrected for instrumental polarisation - using the FORS1 relation in Patat & Romaniello (2006) - it is possible to obtain a self-consistent picture by only using field stars closer to the optical axis and the SN. These result in a consistent determination of the ISP ($Q_{\rm ISP} = 0.42 \pm 0.11\%$, $U_{\rm ISP} = 0.13 \pm 0.09\%$), and are clearly different from the properties of PS15br ($Q_{\rm SN} = 0.78 \pm 0.17\%$ and $U_{\rm SN} = -0.74 \pm 0.14\%$. By correcting for the ISP so evaluated, we obtain a polarisation signal that appears significant $Q = 0.36 \pm 0.20\%$ and $U = -0.87 \pm 0.17\%$, resulting in $P = 0.94 \pm 0.17\%$. After correcting for polarisation bias, according to Patat & Romaniello (2006), this value reduces to $P_0 = 0.93 \pm 0.17\%$. Indicatively,

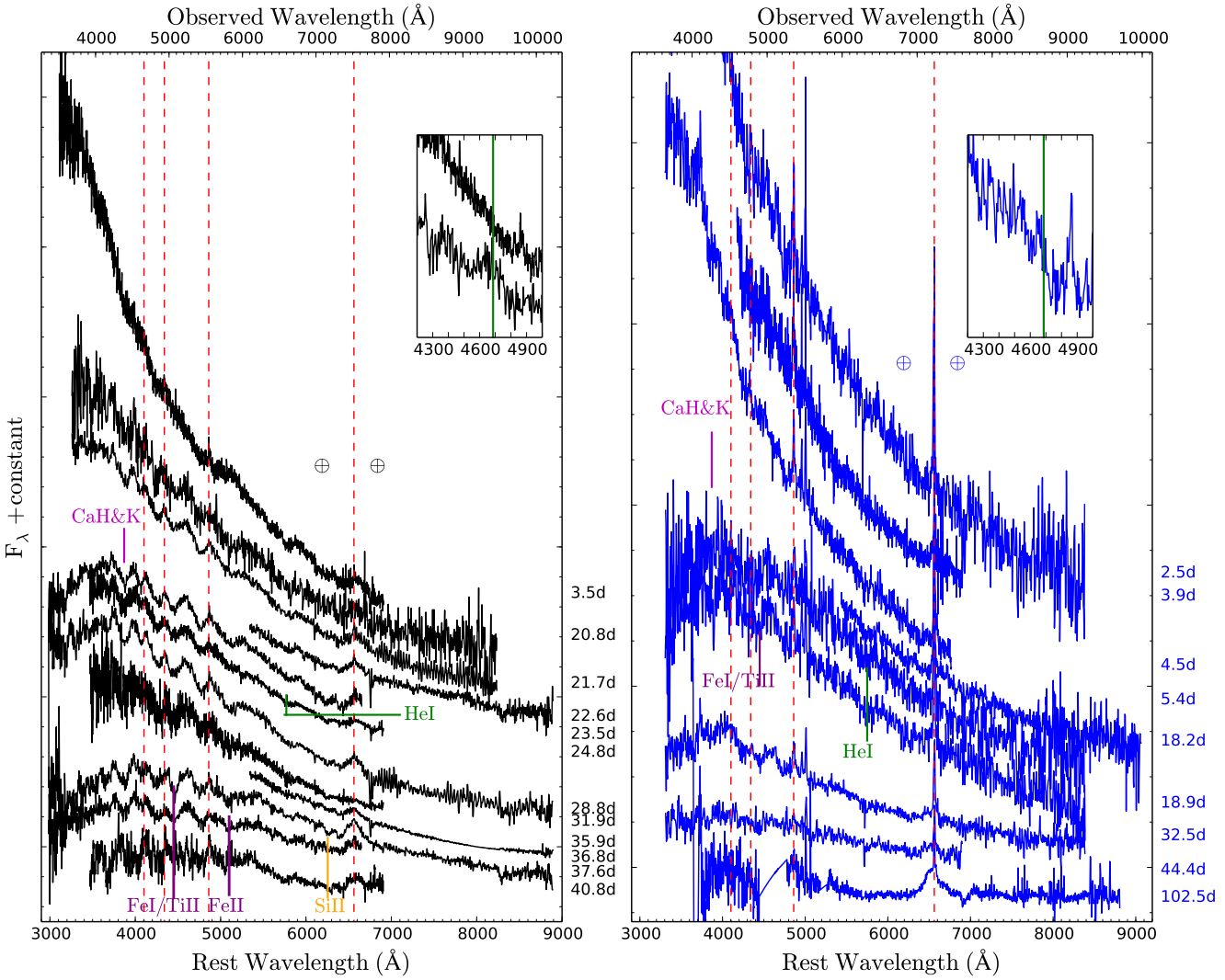

FIG. 8.— Left: photospheric spectra evolution of SN 2013hx. Right: spectra evolution of PS15br. The phase of each spectrum relative to light curve peak in the rest frame is shown on the right. The spectra are corrected for Galactic extinction and reported in the rest frames.The most prominent features are labelled The ⊕ symbols mark the positions of the strongest telluric absorptions. Balmer lines Hα to Hδ are marked with red vertical dashed lines. The insets show a zoom-in of the first spectra in the region around 4600 Å with the rest-frame He II λ4686 marked by a green vertical line. WiFeS spectra were convolved with a factor of five and subsequently binned to a 5 Å scale.

this level of polarisation would correspond to an asymmetry of E $\sim$ 10-15%, assuming an ellipsoidal photosphere (Hoflich 1991). On the other hand, if we assume that all field stars are equally good for the determination of the ISP, we conclude that there is a significant scatter - probably pointing to an unaccounted source of systematic error - and that no conclusive evidence on the source of the polarisation associated with PS15br can de derived. Unfortunately, there are no other suitable stars (bright and not saturated) in the FOV of PS15br to resolve this uncertainty.

7. SPECTROSCOPY

The spectra evolution of the two SNe is shown in Fig. 8 (cfr. Table 12). Both SN 2013hx and PS15br, like SN 2008es (Gezari et al. 2009; Miller et al. 2009), do not show the typical broad absorption features of O II that we see in SLSNe Ic. We note that the spectra have temperatures consistent with the photospheric temperatures at which these ionic transitions are prominent (12000-16000 K, Quimby et al. 2013; Inserra et al. 2013b), even though such ions could be sensitive to non-thermal radiation in a way similar to He I (Mazzali et al. 2016). In general the post peak spectra of both objects show Balmer lines, He, Ca, Fe and other metal lines.

In the earliest spectrum of PS15br there is a feature at 4600 Å that could be associated with C III/N III rather than He II λ4686 (see inset in the right panel of Fig. 8). This feature already weakens in the spectrum at 5 days after maximum. PS15br never shows an Hα absorption component but displays a multicomponent emission profile due to the combination of a relatively broad feature (v$\sim$1500 km s^{-1}) and a narrow component (v$\sim$115 km s^{-1}) which is likely due to the host galaxy since it has a similar width to those of the [O III] emission lines of the host galaxy at λ4959 (v$\sim$96 km s^{-1}) and λ5007 (v$\sim$110 km s^{-1}) as measured from our WiFeS spectrum

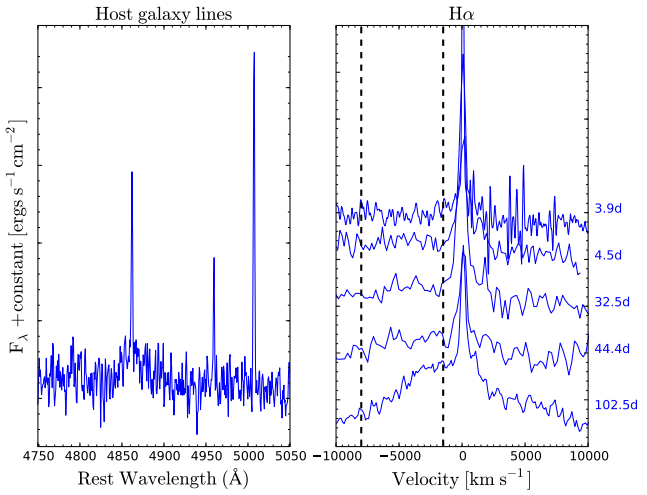

FIG. 9.— Left: zoom in the region where the [O III] host galaxy emission lines are visible in PS15br +3.9d spectrum taken with WiFeS. From left to right the three emissions belongs to Hβ, [O III] λ4959 and [O III] λ5007 due to the host galaxy as inferred from their width. Right: zoom in the Hα region of the early and late spectra. Black vertical dashed lines show the edge of the early 1500 km s^{-1} component and the late 8000 km s^{-1} component.

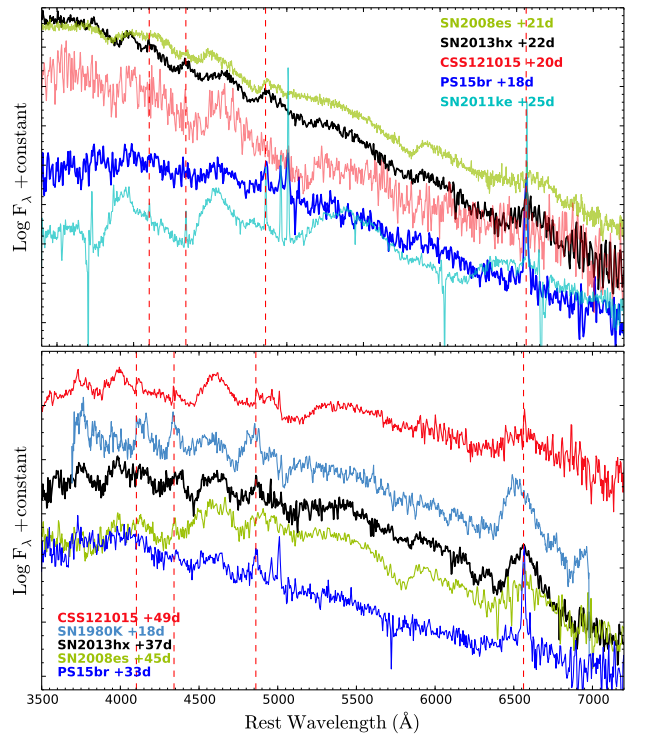

FIG. 10.— Top: comparison of SN 2013hx and PS15br spectra at ∼20 days from maximum with those of SLSNe showing Hydrogen in their spectra SN 2008es (Miller et al. 2009) and CSS121015 (Benetti et al. 2014), together with the H-poor SLSN Ic SN 2011ke (Inserra et al. 2013b). Bottom: Comparison of the spectra of SN 2013hx and PS15br at ∼40 days from maximum together with that of SN 2008es and CSS121015 at similar epoch and that of the type IIL SN 1980K at ∼20 day after maximum light. The spectra of the two SLSNe II are similar to that of the type IIL in the same fashion the SLSNe Ic at ∼30d after maximum resemble normal type Ic at maximum. Hα to Hδ are marked with red vertical dashed lines in all panels.

(see Fig. 9, left panel). Hβ has a similar behaviour although the absorption component is visible from 20 days after maximum. Ca II H&K is visible in the first spectrum and becomes more prominent from day 18 when the metal lines appear as shown by the presence of the Fe II multiplet $\lambda\lambda$4924, 5018, 5169 and possibly Fe I that replaces the 4600 Å feature. He I λ5876 is detectable in the first spectrum and clearly from the third, showing a P-Cygni profile.

The last three PS15br spectra (32 to 102 days) show the appearance of a broad component (FWHM ∼8000 km s^{-1}) at Hα (see right panel of Fig. 9) which is strongly asymmetric in the final spectrum at 102 days. The centroid of the broad Hα feature is somewhat obscured by the narrow galactic emission line, but is certainly blue shifted and we estimate its peak is at -750 km s^{-1}. The asymmetric blue emission is common for Hα of type II SNe and could be due to an opaque core concealing the outermost layers of the receding part of the envelope where the Hα is formed (Chugai 1985) . Alternatively it may be due to a steep density profile of the hydrogen layer, which increases the probability to observe blue-shifted photons since the opacity is mainly due to electron scattering and the line emission mostly comes from the region below the continuum photosphere (Dessart & Hillier 2005; Anderson et al. 2014b).

The absorption to emission ratio of Hα in type II SNe is smaller for brighter and faster declining light curves (Gutiérrez et al. 2014). This phenomenon could be a consequence of the mass and density profile of the hydrogen layer. PS15br spectrophotometric observations fit in this picture. An alternative explanation for the formation of PS15br Hα profile could be related to a weak, early interaction occurring at earlier epochs and responsible for the 1500 km s^{-1} component, whereas the fast SN ejecta would be responsible for the profile of late epochs.

The first spectrum of SN 2013hx at 3 days shows a broad Hα and He I λ5876, while that of 21 days past peak also shows conspicuous Balmer lines and a feature at ∼4600 Å similar to those observed in PS15br and SN 2008es. This feature was also in the first spectrum but apparently weaker. The emission peak of this feature is coincident with He II λ4686, even though a combination with C III/N III cannot be excluded. All the Balmer lines have a P-Cygni profile with the exception of Hα showing only the emission component up to ∼ 30 days after peak. However, the absorption component exhibited by Hα in the +36 to +38 day spectra is weak. Such behaviour resembles that of SNe type IIL. A shallow He I λ5876 line, possibly blended with Na ID, is visible until 40 days after maximum. The Ca H&K lines are visible in all post-peak epochs of SN 2013hx, as well as a feature in absorption at ∼5000 Å likely related to the Fe II multiplet $\lambda\lambda$4924, 5018, 5169. Two other P-Cygni profiles are visible from 20 to 40 days after peak at 3745 Å and 4575 Å which we identify as Fe I. They are possibly blended with Ti II, and Fe II, respectively.

We also note that an absorption feature is shown from +23d to +38d in SN 2013hx (and less clearly from +5d to +19d in PS15br) on the blue side of Hα with an absorption minimum at 6250 Å. This absorption feature has been observed in several type II such as SNe 2007od, 2009bw, 2009dd, 2013ej and 2013by (Inserra et

al. 2011, 2012; Inserra, Baron, & Turatto 2012; Inserra et al. 2013a; Valenti et al. 2014, 2015) at earlier epochs. The two interpretations are high velocity hydrogen originating from interaction between rapidly expanding SN ejecta and a CSM - or Si II λ6355. The latter seems the most plausible identification in our objects since it shows a velocity consistent with, although slightly lower than, other metal lines such as Fe II (see Section 7.1).

The spectral evolution of these objects provides additional information about hydrogen-rich SLSNe. In the top panel of Fig. 10 the comparison of the spectra around +20d post maximum with those of the other SLSNe such as SNe 2008es, 2011ke and CSS121015 highlights a difference in the line evolution between PS15br, CSS121015 and the other two SNe. CSS121015 shows weaker H than SNe 2013hx and 2008es with $\mathrm{EW(H}\alpha)_{\mathrm{SN2013hx,SN2008es}} \sim 10 \times \mathrm{EW(H}\alpha)_{\mathrm{CSS121015}}$. CSS121015 also exhibits Fe II lines which are more prominent than the other type II SLSNe at similar phase. Indeed the Fe absorption lines in CSS121015 are stronger than those of SLSNe II SN 2013hx, PS15br and SN 2008es with $\mathrm{EW(Fe)}_{\mathrm{CSS121015}} \approx \mathrm{EW(Fe)}_{\mathrm{SLSNeIc}} \sim 5 - 10 \times \mathrm{EW(Fe)}_{\mathrm{SLSNeII}}$. Both SN 2013hx and PS15br are also different from typical SLSNe I spectra. These show the same metal lines observed in CSS121015 at similar epochs. The difference between SLSNe I, dominated by broad metal lines, and SLSNe II, exhibiting H lines with weaker metal lines with respect to the SLSNe I, is highlighted in the top panel of Fig. 10.

In the bottom panel of Fig. 10 we compare the spectra of SN 2013hx and PS15br with those of the other two SLSNe II at 40 days, together with that of the type IIL SN 1980K[34] at 20 days past maximum light. There is some resemblance between SN 2013hx, SN 2008es and SN 1980K spectra with similar features redwards of Hβ. At these epochs SNe IIL exhibit $v \sim$8200 km s^{-1} components in Hα while SN 2013hx shows $v \sim$8000 km s^{-1}. Similar trends are visible for Hβ, with $v(\mathrm{H}\beta)_{\mathrm{SN1980K}} =$ 7400 km s^{-1}, which is similar to $v(\mathrm{H}\beta)_{\mathrm{SN2013hx}} =$ 7200 km s^{-1}. In addition, the strength of the He I λ5876 line is similar between the objects ($\mathrm{EW_{SN1980K}} =$ 10Å compared to $\mathrm{EW_{SN2013hx}} =$ 11Å, while $\mathrm{EW_{SN2008es}} =$ 18Å). This also holds true for the Fe II feature (multiplet 52), which has $\mathrm{EW_{SN1980K}} =$ 16Å and $\mathrm{EW_{SN2013hx}} =$ 18Å. Blueward of Hβ the profiles begin to differ to some extent, mainly due to Fe I/Ti II shown around 4000 Å in SLSNe and a stronger Ca H&K ($\mathrm{EW_{SLSNeII}} \sim 2 - 3 \times \mathrm{EW_{SN1980K}}$) The line profiles for PS15br are more similar to those of SN 2013hx and SN 2008es than those of CSS121015. Benetti et al. (2014) claimed a possible connection between CSS121015 and luminous type IIn such as SNe 1997cy and 2012ca (Turatto et al. 2000; Inserra et al. 2014, 2015b, and reference therein) but PS15br does not show a blue pseudo-continuum that characterises those IIn spectra. Indeed, in the spectrum bluewards of Hα, PS15br is similar to SN 2013hx and SN 2008es in line strength. CSS121015 also shows some similarities to type IIL but the hydrogen emission is weaker, and the Fe II and Mg II are more prominent. Of the four objects, CSS121015 displays the weakest hydrogen emission lines.

[34] Some of such spectra were digitalised and flux calibrated in Benetti PhD thesis, 1992.

7.1. *Expansion velocity and temperature*

The expansion velocities for our SNe, as inferred from the position of the minima of the P-Cygni profiles for Hα and Fe II (multiplet 52), are compared with those of SLSNe Ic, type II SNe, SLSN II SN 2008es and SLSN CSS121015 (right panel of Fig. 11). The errors were estimated from the scatter between several independent measurements. In the case of Hα, the velocities were computed from the FWHM of the emission lines for PS15br and for SN 2008es in spectra after 40 days. Hα velocities decline monotonically from 12000 km s^{-1} to 7500 km s^{-1} on the time scale available for SN 2013hx. An almost identical decrease is observed in SN 2008es and PS15br in the available period (20 < phase (day) < 45) even if PS15br values are due to the broad emission component. The decline rate is qualitatively similar to normal luminosity type II (plateau and linear) SN which have average velocities which are lower by about 1200 km s^{-1} at similar epochs, whereas SN 1980K Hα velocity evolution resembles those of SLSNe II. The velocities measured from the FWHM of the emission components appear to be systematically higher than those inferred from the minima. The Fe II velocities are usually assumed to be better tracers of the photospheric velocity and these are are similar in SNe 2013hx, 2008es and PS15br. These show the same decline as displayed in normal type IIL, but with a shift or delay by of ∼15-20 days. The SLSNe II Fe II velocities are quite different to SLSNe Ic, in that they are ∼7000 km s^{-1} slower.

In the left panel of Fig. 11 the evolution of the temperature is plotted. It is derived from the blackbody fit to the continuum of our spectra (square symbols) and color temperatures at rest-frame (dot symbols). Only SN 2013hx has multi-band coverage before peak allowing us to estimate the temperature pre-peak (17000 to 15000 K). SN 2013hx shows a monotonic decline from 14000 K at peak to 6600 K at 40 days, while PS15br declines from 12000 K to 6000 K showing similar temperatures to SN 2013hx and SN 2008es in the same time coverage. After 50 days, the temperatures of the objects tend to flatten at ∼5500 K. SN 2008es shows a similar temperature evolution to that of SN 2013hx, while CSS121015 is 3000 K hotter at peak than SLSNe II. The overall temperature evolution of SN 2013hx, PS15br and SN 2008es is between those observed in SLSNe Ic and type II SNe with a similar decline to those of type II.

7.2. *SN 2013hx late time spectra and signs of interaction*

In Fig. 12 we show the late VLT+FORS2 spectrum of SN 2013hx together with the K-corrected photometry, which is the latest spectrum and the only one in the late (>150d from peak) phase for a SLSN II obtained to date. As described in Section 3, this is a total of 4hr15min exposure on VLT+FORS2 at an epoch of +237d past maximum (rest frame), when the SN has $r = 23.2$ mag (see Table 6). A lower signal-to-noise spectrum was taken by PESSTO on +210d, and is also shown in Fig. 12. This NTT spectrum does not appear to be significantly different to the FORS2 +237d spectrum and as it is much lower quality, we will not discuss it further.

There is no distinguishable line at the position of [O I] $\lambda\lambda$6300, 6364Å, which is usually prominent in core-

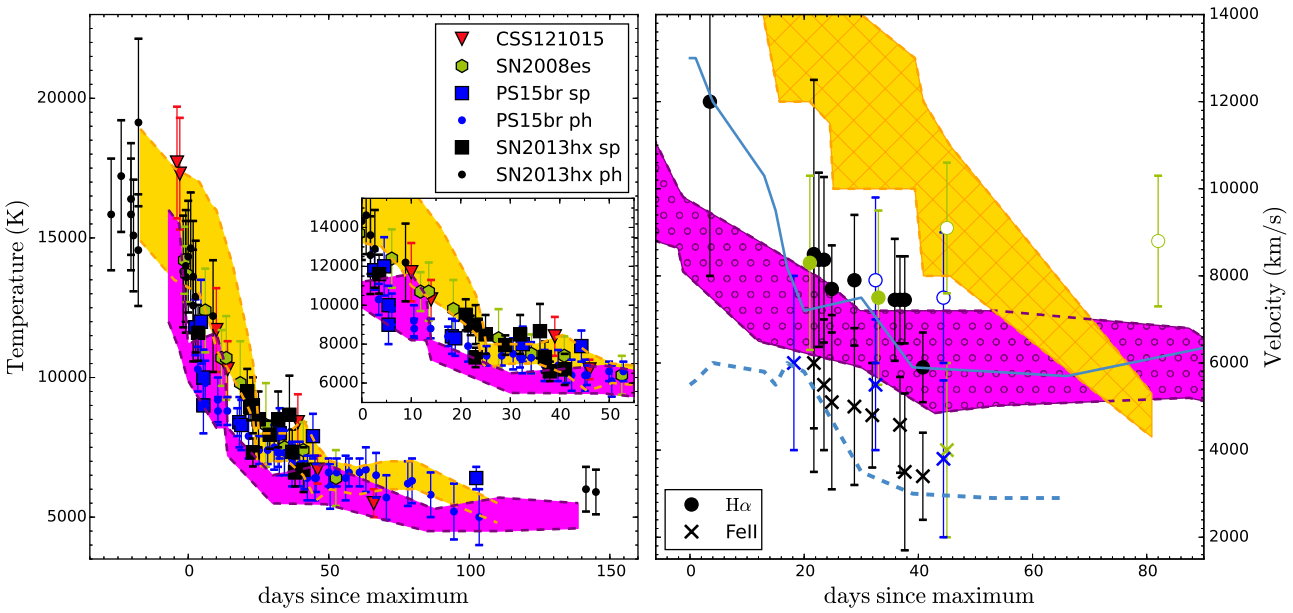

FIG. 11.— Left: SN 2013hx (black) and PS15br (blue) temperature evolution compared with those of SLSN II 2008es (green) and the SLSN CSS121015 (red). The gold region represent the temperature space of SLSNe Ic (Inserra et al. 2013b; Nicholl et al. 2014), while the magenta that of a type IIP/L collection (SNe 1979C, 1999em, 2004et, 2007od, 2009bw, 2009dd, 2009kf, 2012A; Barbon et al. 1982; Elmhamdi et al. 2003; Maguire et al. 2010; Inserra et al. 2011, 2012, 2013a; Botticella et al. 2010; Tomasella et al. 2013). An inset with the zoom of the evolution between peak and 50 days is also shown. Right: Hα and Fe II (multiplet 52) evolution of SN 2013hx (black) and PS15br (blue) compared with that of SN 2008es (green), the type IIL SN1980K (solid light blue line for Hα and dashed for Fe II; Barbon, Ciatti, & Rosino 1982). The gold crossed region represents the velocity space of Fe II line in SLSNe Ic, while the circled magenta that of Hα in type IIP SNe. Open symbols refer to velocities computed with the FWHM of the emission lines.

collapse supernovae. There is perhaps some hint of weak and broad emission that could be attributed to this line, but the the detection is $\lesssim 2\sigma$ with respect to the continuum flux and is not convincing. We compared our spectrum with those of the bright type II SN 1980K (Barbon, Ciatti, & Rosino 1982) and the broad-line type Ic SN 1998bw (Patat et al. 2001) at late epochs and scaled to the same luminosity distance of SN 2013hx (570.3 Mpc) in order to match the rest-frame spectral luminosity exhibited by SN 2013hx. The spectra of SN 2013hx and SN 1980K shown in Figure 12 are similar, although they differ by 135 days with respect to the peak epochs. Although the [O I] line is weaker than that displayed in SN 1998bw, the overall similarity with type IIL SNe suggest that also SLSNe II are consistent with a massive star explosion. The Hα profile and the blueward features are also different from that of iPTF13ehe (Yan et al. 2015), while the width of the central component of SN 2013hx Hα (see Tab. 3) is comparable with that of PS15br at $\sim$100d.

The +247d spectrum is dominated by a strong and multicomponent Hα profile, and the simplest explanation would be that the SN ejecta is interacting with an H-rich, highly asymmetric CSM. There are no other lines visible with the exception of a weak Hβ, and the continuum is faint. The Hβ flux is $\sim$50 times less than that of the Hα profile and $\sim$30 times less than Hα central component (see Tab. 3). For case B recombination in the temperature regime $2500 \leq$ T(K) ≤ 10000 and electron density $10^2 \leq n_e \leq 10^6$ the Hα line should be 3 times stronger than Hβ. However, the case B recombination is never observed in type II SNe before a couple of years since both the $n = 4 \rightarrow n = 2$ (Hβ) and $n = 3 \rightarrow n = 2$ (Hα) transitions are optically thick (Xu et al. 1992). In this case the Pα ($n = 4 \rightarrow n = 3$) transition will depopulate the $n = 4$ state, with the photons escaping to produce the visible Pα emission line. Hα however is produced strongly as the only other alternative for depopulation of the the $n = 3$ state is Lyman β. The integrated luminosity of the overall profile of Hα line is $\sim$9 times those of a normal type II at similar phase (Kozma & Fransson 1998) suggesting an additional contribution to Hα luminosity. What powers the decline rate of the late time light curve is an open question. One could speculate that the signature of interaction we see at this late phase is indicative of the same powering source for the light curve between 100−260 days. Late interaction has been observed in bright type IIL such as SNe 1979C, 1980K and 1986E (Fesen et al. 1999; Cappellaro, Danziger, & Turatto 1995; Benetti et al. 2016, and references therein).

The Hα profile in Fig. 13 has a triple peak structure spanning 7400 km s^{-1} across the base (cfr. Tab 3), which is similar to the triple peak shown by PTF11iqb after 500 days (Smith et al. 2015). The central component is consistent with having zero rest-frame velocity, and the blue component peaks at -4700 km s^{-1} with respect to this Hα rest-frame velocity. This blue component appears to be the weakest of the three. The red component is at $+4000$ km s^{-1}. We analysed the feature with gaussian, lorentzian and pseudo voigt line profiles having set *a priori* the number of components (three) but letting vary the width and intensity of each component. We retrieved the best fit with three voigt profiles with widths of $\sim$3400 km s^{-1}. However Gaussians have a similar goodness of fit

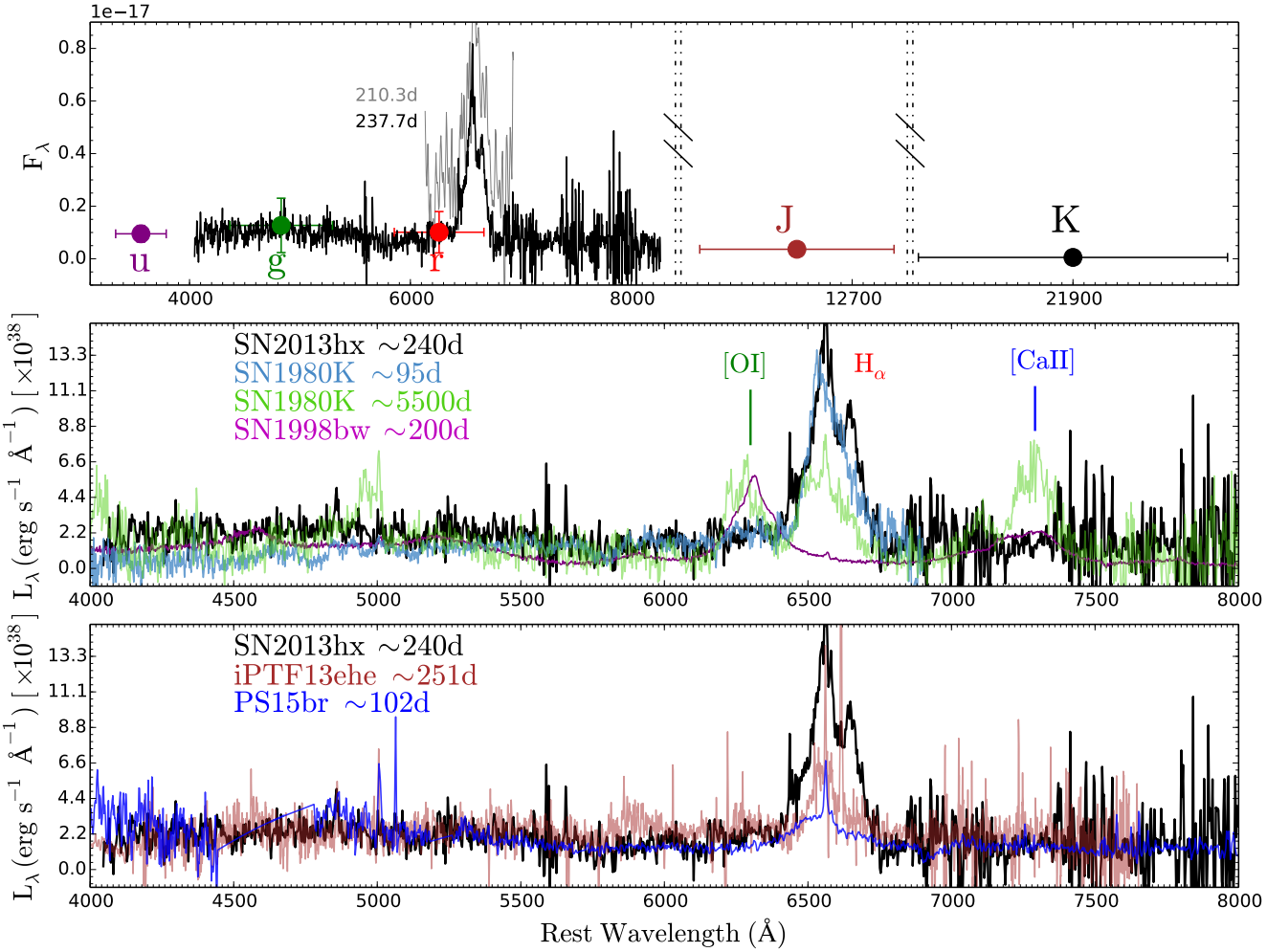

FIG. 12.— Top: Last two spectra of SN 2013hx together with the K-corrected photometry (filled symbols) at close epochs, optical at +257d and NIR at +266d with respect to maximum light. Middle: the VLT+FORS2 spectrum of SN 2013hx compared with late spectra of the type IIL SN 1980K and a late spectrum of the broad-line type Ic SN 1998bw. All the spectra have been scaled to the continuum flux level of SN 2013hx. The most prominent line of nebular core-collapse spectra are labelled. Bottom: the VLT+FORS2 spectrum of SN 2013hx compared with the last spectrum of PS15br and the SLSNe Ic iPTF13ehe, which is the only H-free SLSNe showing a late Hα emission.

and produce similar line widths but somewhat different line fluxes.

The line profile could be schematically explained by:

1. a relatively broad emission from the SN ejecta with FWHM ∼3400 km s^{-1};
2. interaction of the H-rich ejecta with:
   (a) a ring/disk edge-on,
   (b) a dense, clumpy CSM;
3. a likely unshocked CSM that could explain the narrow, unresolved emission on the top of the central component.

The blue wing of the Hα emission of SN 2013hx roughly coincides in wavelength with the corresponding blue wing of the Hα profile at 37 days as shown by the top panel of Fig. 13. If the absorption minimum maintains the same velocity shown at 38 days post peak, it will be at a similar wavelength to the peak of the blue component. However, if SLSNe II evolution follows closely that of bright type II as suggested by the spectroscopic evolution (see Section 7 and bottom panel of Fig. 12), we would not expect any absorption component from the Hα able to dim the blue peak. Instead an asymmetric, clumpy CSM could explain the difference in intensity between the blue and the red component. If we considered the blue component to be a consequence of a boxy profile, and hence more a shoulder than a peak, we would still need to invoke an asymmetric configuration. Such CSM structure would have a two-component wind with a spherically symmetric region responsible for the boxy profile and the presence of a denser clump in the direction opposite to that of the observer in order to explain the intensity of the red component. Hence both the scenarios would suggest an asymmetric configuration of the CSM. Such configurations have been invoked to explain late time multicomponent Hα profiles for several type II SNe (e.g. Uomoto & Kirshner 1986; Fesen et al. 1999; Pozzo et al. 2004; Inserra et al. 2011; Benetti et al. 2016).

8. DISCUSSION

TABLE 3
Late (∼240 day) Hα profile of SN 2013hx.

Feature	Peak (Å)	Width (Å)	Width ($km\,s^{-1}$)	Velocity w.r.t. Hα peak ($km\,s^{-1}$)	Flux ($erg\ s^{-1}\ cm^{-2}$)
Blue	6459.8	73.8	3427	−4700	1.1×10^{-16}
Central	6558.9	73.8	3376	−190	4.0×10^{-16}
Red	6650.8	73.8	3329	4000	2.2×10^{-16}

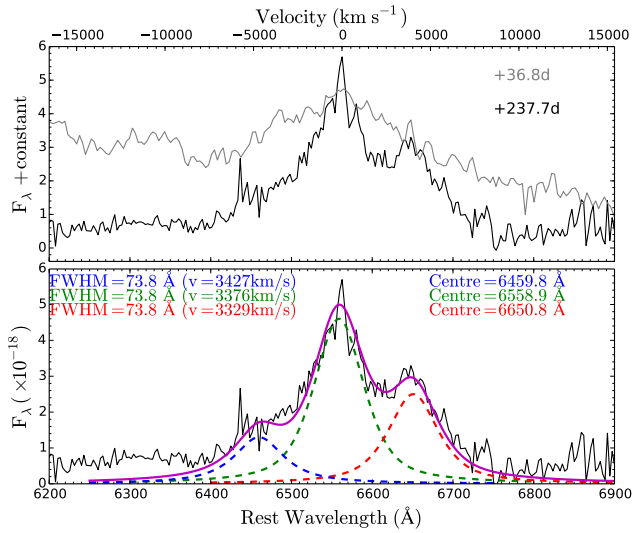

Fig. 13.— Top: Hα multicomponent profile of the spectrum at 238 days (black line) with that exhibited at 37 days (grey line) scaled in flux to match the previous spectrum. Bottom: Hα multicomponent profile of the spectrum at 238 days since maximum. The spectrum is dominated by interaction with a H-rich CSM.

Thanks to the discovery and follow-up of SN 2013hx and PS15br we have, for the first time, a small sample of SLSNe II that provide new data for the understanding of the hydrogen-rich superluminous SNe. These SNe are different than those undergoing strong interaction with an optically thick CSM showing spectra with strong optical lines having multiple emission components such as SN 2006gy (Smith et al. 2007). They have luminosity spanning from $-20 > M_g > -22$, similar spectral evolution and an origin in faint host galaxies. The latter is similar to the characteristic locations of their hydrogen-free counterparts (Lunnan et al. 2014; Leloudas et al. 2015; Chen et al. 2015). Their spectroscopic evolution resembles those of type IIL SNe with a delay of 15-20 days and their light curves show a linear decline over 100 days post peak. Hence they are more luminous and evolve more slowly than normal type IIL SNe. These two characteristics (more luminous, slower evolution) also link SLSNe I to normal type Ic SNe in a similar way. Therefore it may be that an additional power source that distinguishes a SLSN II from a normal SN II is the same as that which distinguishes SLSNe I from normal SN Ic.

The extreme luminosity of SLSNe I and Ic have been explained with a few scenarios and we use our extensive dataset to constrain similar models for the origin of these SLSNe II. Of particularly use are the measurements of the bolometric luminosity, and the temperature and velocity information. To be clear, the light curves that we will use in the following Sections are the full, estimated, bolometric light curves that have been corrected for flux missed in *both* UV and NIR as described in Section 5.

8.1. ^{56}Ni *driven explosion*

To test if radioactive heating could be the main source of energy, we can assume that γ-rays from ^{56}Co decay are fully thermalized and can hence estimate the ^{56}Ni mass needed for these events comparing their bolometric luminosity with that of SN 1987A. For SN 2013hx, the peak would require a ^{56}Ni mass of $M(^{56}\mathrm{Ni})\sim 8.0\ M_\odot$ and the luminosity in the tail phase at around 140 days would be $M(^{56}\mathrm{Ni})\sim 1.0\ M_\odot$. For PS15br, the luminosity at 100 days would require $M(^{56}\mathrm{Ni})\sim 2.2 M_\odot$. Although these objects are H-rich and hence hydrogen recombination should play some role in the photospheric phase of the light curve, we applied our toy model (see Appendix D of Inserra et al. 2013b) to have an alternative estimate of the ^{56}Ni mass required to power the late light curves. We retrieved values of $4.3 < M(^{56}\mathrm{Ni}) < 8.4 M_\odot$ for SN2013hx (depending on whether or not we included the tail phase data after 142 days) and $M(^{56}\mathrm{Ni})\sim 4.4 M_\odot$ for PS15br.

Although there is some uncertainty in these numbers, the large ^{56}Ni masses require and imply a pair instability explosion (Barkat et al. 1967; Fraley 1968). As a consequence of the large ejecta masses in pair instability explosions, the rise times of the light curves should be a factor 2-3 greater than that observed in our objects as shown in (Woosley et al. 2007; Kasen et al. 2011) and as demonstrated for SLSN I (Nicholl et al. 2013). In addition, the ejecta masses should be 2-5 times greater than the ^{56}Ni mass (Umeda & Nomoto 2008), so as the spectra would not be dominated by Fe-group elements. However, following the findings of Woosley & Weaver (1995) such amount of material would be mainly composed of He ($> 13 M_\odot$) and H ($> 11 M_\odot$) leading to a long plateau in their light curves, which has not been observed. This implies that the light curve of SN 2013hx after 140 days is not driven by ^{56}Ni but is due to some late interaction - as suggested in Section 7.2 - which is mimicking the ^{56}Co to ^{56}Fe decay. This phenomenon has previously been observed in other normal type II SNe (e.g. Andrews et al. 2010; Inserra et al. 2011).

8.2. *Circumstellar medium interaction*

In SN 2013hx, PS15br and SN 2008es we do not observe narrow and intermediate features suggesting an ongoing interaction with a CSM. However, we cannot exclude a priori such scenario since if the CSM is opaque and the shock encounters no further CSM at larger radii,

the usual signatures of interaction spectra can be avoided (Smith & McCray 2007; Chevalier & Irwin 2011). This could, in principle, explain the spectra evolution in the the objects.

The dense CSM can be produced by a wind or by a shell ejected prior the SN explosion. In the former case, following the model of Blinnikov & Bartunov (1993) used to explain type IIL, a dense stellar wind that reprocesses the UV photons produced at shock breakout can boost the luminosity up to superluminous magnitudes. That would need an increase in the mass-loss rate by one to two orders of magnitude, with respect to those observed in red supergiant (RSG) and hence reaching $\dot{M} \sim 10^{-3}$ $M_\odot$ yr^{-1}. However, in this scenario after $\sim 50-80$ days from peak, the light curve should show a drop in magnitude. The higher the peak luminosity, the greater the drop with at least a decrease of two mag in a superluminous case - and a subsequent settling onto a ^{56}Co tail. Our dataset, including SN 2008es, does not show such a drop around that phase or even later.

From the blackbody fit to the SED (see Section 7.1) and the bolometric luminosity (see Section 5), we can estimate the peak radius of SN 2013hx and PS15br to be 3×10^{15} cm and 2.3×10^{15} cm, respectively. These radii are a factor 30 and 10 greater than that of a large RSG (Smith et al. 2001) and as a consequence the opaque CSM shell forming the envelope is not bound to the star. Following the formalism of Quimby et al. (2007); Smith & McCray (2007), the peak luminosity produced by the radiation emitted by a shocked, thermalized shell is

$$L \propto \frac{M_{sh} v_{ph}^2}{2\, t_{max}}, \quad (1)$$

where M_{sh} is the mass of the dense CSM shell, v_{ph} is the velocity of the pseudo-photosphere and t_{max} is the rise time. Assuming a rise time of 37 days for SN 2013hx and 35 days for PS15br (cfr. Section 4) and a pseudo photosphere of 6000 $km\,s^{-1}$ (cfr. Section 7.1) we can infer 2.5 $M_\odot$ and 0.5 $M_\odot$ for the CSM masses of SN 2013hx and PS15br, respectively.

The aforementioned radii imply a wind distance of 300 and 150 AU for the two objects and inferring a wind velocity of 10-100 $km\,s^{-1}$ (which brackets RSG and faster luminous blue variable wind velocities), the wind must have begun ∼10-100 yr before the explosion of SN 2013hx and ∼7-70 yr before that of PS15br. Hence, the mass-loss rates would be 0.03-0.25 $M_\odot$ yr^{-1} and 0.007-0.07 $M_\odot$ yr^{-1}, which are too large to be produced by a normal steady stellar wind. Therefore if a a dense CSM scenario is invoked as the explanation of the peak luminosity, it would suggest that an unbound CSM shell configuration.

In order to reproduce the bolometric light curve of SN 2013hx, PS15br and also SN 2008es we use a semi-analytic code based on the equations of Chatzopoulos et al. (2012) and implemented by Nicholl et al. (2014). We use the model considering both CSM shell and radioactive decay of ^{56}Ni contribution to the light curves, setting $\delta = 2$ and $n = 12$ for the SN ejecta inner and outer power-law density profile slopes, respectively, in all cases. We assume Thomson scattering to be the dominant source of opacity with a solar mixture of mass fraction ($X = 0.7$), which gives an opacity $\kappa = 0.2(1 + X) = 0.34$ cm^2 g^{-1} that is the standard value for a hydrogen and helium rich ejecta. An identical configuration was previously used by Chatzopoulos et al. (2013) to fit the bolometric light curve of SN 2008es. Our best fits are shown in Fig. 14 (red dot-dashed line), while their parameters are reported in Table 4. Since the late SN 2013hx tail may be dominated by interaction - with a different and probably less dense component see Section 7.2 - we made two illustrative fits. First, we fitted the light curve using data up to 40 days after maximum and then a second using all data out to 178d (before the clear inflection in slope; see Sections 4 & 5) and before the first spectrum showing interaction with another CSM (at 210d, see Section 7). We derive $2.1 \lesssim M_{CSM} \lesssim 2.7\,M_\odot$, $0.0 \lesssim M(^{56}Ni) \lesssim 2.0 M_\odot$ and $9.5 \lesssim M_{ej} \lesssim 12.9 M_\odot$. Following the same methodology we also estimate that a wind of 2.6 $M_\odot$ (or 4.7 $M_\odot$ in case of dense shell configuration) is responsible for the late interaction of SN 2013hx. The ^{56}Ni masses are consistent with the aforementioned limit and the CSM mass is consistent with observation of a pseudo-photosphere at the velocity reported in Section 7.1. This mass is of the order of that associated with impulsive mass ejections as discussed in Smith & Owocki (2006). However, the ejecta masses are at least a factor two greater than what is expected to avoid an optical plateau from hydrogen recombination, while the total masses (ejecta+CSM+remnant) lie in the upper end of those observed and theorised for type II SNe (Smartt 2009, 2015; Janka 2012). On the other hand, such CSM masses are more similar to those of stripped envelope SNe and not of type II. This two component wind CSM configuration that is required to explain the late interaction of SN 2013hx, is obviously difficult to explain with a single steady wind.

8.3. *Internal energy source*

Despite the potential of the CSM scenario to describe the main observational data - light curves and spectra evolution - and the overall picture observed in SLSNe II, there are still some details that would be easier to explain with a central engine that deposits its energy into a supernova explosion and significantly enhance the luminosity.

As observed in Section 5, PS15br has an asymmetric light curve may be difficult to explain with a CSM interaction, as also shown in Fig. 14. In addition SLSNe II have bell shaped light curves around peak only a factor 1.2 wider than those of SLSNe I. Furthermore, they show similar spectra and temperature evolution to those of bright type II SNe but delayed by 15-20 days in a similar fashion to what shown between SLSNe I and stripped envelope SNe. In addition they share similar faint host galaxies as those of SLSNe I.

For these reasons we fit our light curves with our semi-analytical diffusion model presented in Inserra et al. (2013b) in which a rapidly spinning magnetar deposits its rotational energy into a supernova explosion, through magnetic dipole radiation, and significantly enhances the luminosity [35]. Then, we treat for γ-ray leakage from ejecta as done in Chen et al. (2015), which is similar to the prescription of Wang et al. (2015). The magnetar luminosity depends primarily on two parameters,

[35] The semi-analytical code is available at `https://star.pst.qub.ac.uk/wiki/doku.php/users/ajerkstrand/start`

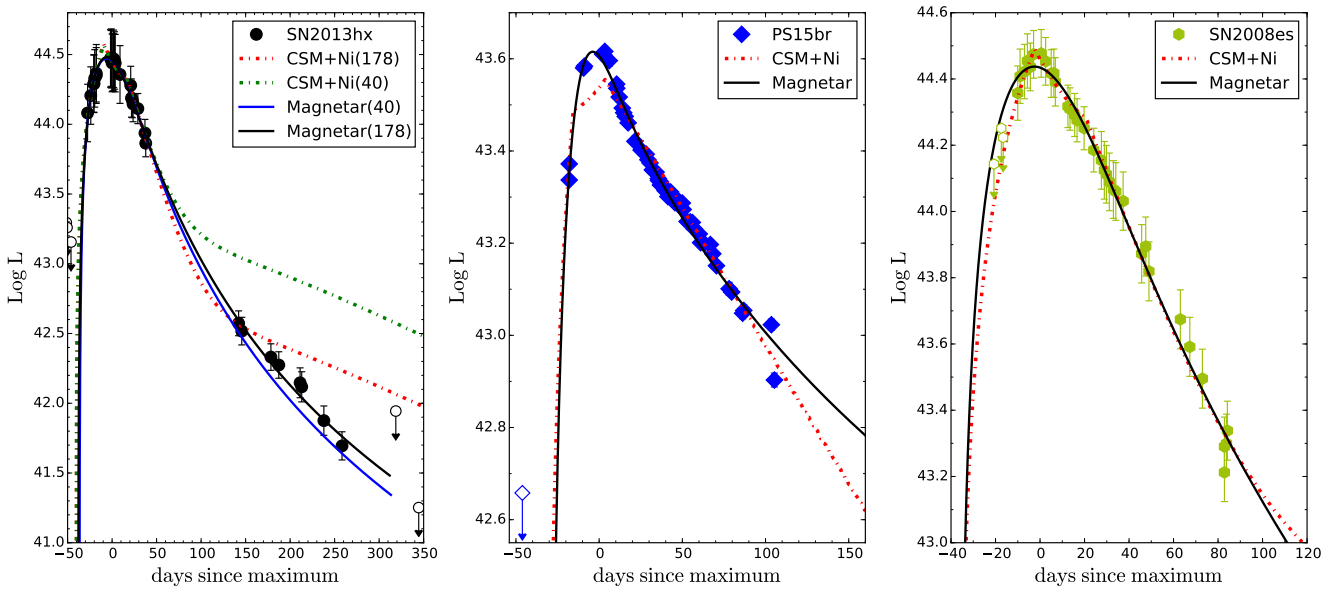

FIG. 14.— Bolometric light curves of SN 2013hx, PS15br and SN 2008es compared with the best-fit models. The black solid line (and also the blue for SN 2013hx) refers to the magnetar model, while the red dot-dashed (and also the green for SN 2013hx) refers to the CSM+Ni model. Limits are shown as empty symbols. For the case of SN 2013hx, the (40) models consider up to 40 days past maximum, while the (178) refer to the models considering up to 178 days.

TABLE 4
BEST-FIT PARAMETERS FOR THE CSM+NI MODEL.

Object	t_{rise} (days)	M_{CSM} ($M_\odot$)	M (^{56}Ni) ($M_\odot$)	M_{ej} ($M_\odot$)	χ^2
SN 2013hx*	40.35/40.35	2.35/2.37	2.02/0.61	9.81/10.48	0.04/0.04
PS15br	31.90	2.09	0.00	12.94	9.10
SN 2008es	36.41	2.75	1.14	9.46	0.18

∗ The first values refer to the model considering only the first 40 days, while the second refer to the model considering up to 178 days.

TABLE 5
BEST-FIT PARAMETERS FOR MAGNETAR MODELLING OF THE BOLOMETRIC LIGHT CURVES AND χ^2 VALUE ON THE LEFT. DERIVED PARAMETERS ON THE RIGHT.

Object	τ_m (day)	B_{14}	P_{ms}	t_0 (MJD)	χ^2	E^{mag} (10^{51} erg)	M_{ej} ($M_\odot$)
SN 2013hx *	36.71/38.15	1.31/0.89	2.22/2.29	56643.20/56641.57	0.04/0.07	3.38/5.24	6.95/5.20
PS15br	17.60	1.61	6.38	57056.27	3.23	0.39	1.93
SN 2008es	36.58	0.97	2.35	54578.28	0.20	2.66	5.71

∗ The first values refer to the model considering only the first 40 days, while the second refer to the model considering up to 178 days.

the magnetic field strength B_{14} (expressed in terms of 10^{14}G) and the initial spin period P_{ms} (in milliseconds). As previously done with the interaction model, we used an opacity $\kappa = 0.34$ cm^2 g^{-1}. Table 5 lists the best-fit parameters for each object, and Fig. 14 shows the fits (black solid line). As the χ^2 fitting gives good matches to models *without* ^{56}Ni, we have no need to introduce ^{56}Ni as an additional free parameter. As in the case of CSM model fitting for SN 2013hx, we do two fits (only using data up to 40 days and then using all data up to 178 days), which in this case are very similar. The light curves of our two objects are quite well reproduced but the late luminosity of the model for SN 2013hx is better reproduced by the 40 days magnetar model. These data points may already have an additional luminosity contribution due to some late interaction (as seen in the late spectra), and hence a light curve dimmer than these points would favour such a model. On the other hand, the CSM models are too bright to describe SN 2013hx data after ∼180 days. Furthermore if we remove the ^{56}Ni contribution, we get a worse χ^2 and a luminosity at late time still brighter than the data. The magnetar fit for PS15br is better than that of the CSM as testified by the χ^2 values of Tables 4 & 5, despite the latter having a higher number of free parameters. The magnetar fit to SN 2008es is not as satisfactory as the CSM one, as the data show a faster rise than the best fit model. One may

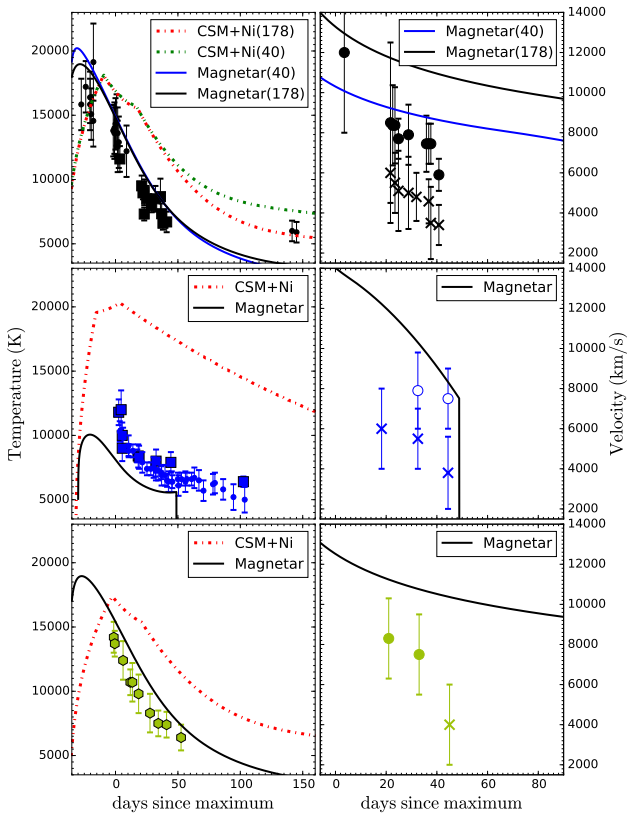

FIG. 15.— Bolometric light curves of SN 2013hx, PS15br and SN 2008es compared with the best-fit models. The black solid line (and also the blue for SN 2013hx) refers to the magnetar model, while the red dot-dashed (annd also the green for SN 2013hx) refers to the CSM+Ni model. Limits are shown as empty symbols.

ask why SN 2013hx and SN 2008es end up with different results if their light curve behaviour is so similar. The reason is that we have different time coverage for each. The light curve data for SN 2008es stretch to 80 days after peak where as the data for SN 2013hx stops at 50 days, and there are more pre-peak detection points for SN 2013hx than for SN 2008es (which has only limits before -10 days).

We further estimated velocity and temperature evolution from the light curve fits to ejecta mass and kinetic energy. In Fig. 15 we show that the temperature evolution of the magnetar model matches the observed ones reasonably well and better than the interaction model, which produces results which are always too hot. Photospheric velocities are consistent with or slightly faster than the data. The sudden drop to zero of both temperature and velocity evolution of the best fit model for PS15br happens because more than half of the core has been exposed. This is a consequence of the low energy and ejecta mass needed to fit the light curve.

Another possible central engine is that of the fall-back accretion (Dexter & Kasen 2013), which can give a similar asymptotic behaviour of the light curve ($L_t \propto t^{-5/3}$) with respect to the magnetar engine but would have lower luminosity than that observed after 180 days in SN 2013hx. However, this scenario implies photospheric velocities higher than that shown by our sample and would fail to reproduce PS15br light curve since models considering H recombination have longer rise times and a bump 200 or 300 days after the explosion. To better investigate this scenario a dedicated fit for these objects is required.

8.4. *SLSN II host galaxies*

Although our sample is small, it offers the first possibility to compare the host galaxy properties of SLSNe II to those of SLSNe Ic.

The likely host galaxy of SN 2013hx, offset by 2″ from the supernova (which we called Host A in Section 2.1) has $M_r = -15.58 \pm 0.16$ mag. If the true host is actually the faint flux (3σ significance) which was detected in the Magellan image, closer to the SN position, then it would be $M_r = -14.81 \pm 0.35$ mag. The deep FORS2 spectrum is dominated by interaction and hence a clean measurement of the galactic Hα is not possible to provide a reliable star formation rate (SFR). As alternative, we measured the flux of Hβ and assumed case B recombination with $T_e = 10^4$. We caution that this emission is measured from the spectrum of the extracted SN 2013hx, and may not be fully or exclusively that of the Host A. To clear up this ambiguity, a deep spectrum of both the possible hosts would be necessary. Nevertheless, we measured a flux $F(H\beta) = 1.29 \pm 0.12 \times 10^{-17}$ erg s^{-1} cm^{-2} which, given the distance luminosity of 570.3 Mpc (see Section 2) corresponds to an inferred $L(H\alpha) = 1.4 \pm 0.6 \times 10^{39}$ erg s^{-1} and a star formation rate $SFR = 11.3 \times 10^{-3}$ M$_\odot$ year^{-1}, applying the calibration of Kennicutt (1998).

The host of PS15br is brighter than that of SN 2013hx, having $M_r = -16.25$ mag. The measurement of the Hα or Hβ flux is also problematic since our available spectra are dominated by SN contribution. We measured the narrowest Hα component of our highest resolution spectra, with an average of $F(H\alpha) = 1.9 \pm 0.7 \times 10^{-15}$ erg s^{-1} cm^{-2} which corresponds to $L(H\alpha) = 4.8 \pm 1.6 \times 10^{40}$ erg s^{-1} and hence a star formation rate of $SFR = 37.7 \times 10^{-2}$ M$_\odot$ year^{-1}. These values should be considered as upper limits as there could be contamination by the SN.

For SN 2008es, no host detection (or emission line measurement) was reported by Miller et al. (2009); Gezari et al. (2009), down to $m_r \sim 23$ mag. However in deeper HST imaging Angus et al. (2016) detected the host at $R = 25.96 \pm 0.20$, which corresponds to $M_R = -13.9 \pm 0.2$. Benetti et al. (2014) detected the host of CSS121015 at an absolute magnitude of $M_r = -18.04$. A limit on the Hα flux of $F(H\alpha) < 4.9 \times 10^{-17}$ erg s^{-1} cm^{-2} was also reported, equivalent to a $SFR < 9.6 \times 10^{-2}$ M$_\odot$ year^{-1}. Hence the hosts span a large range in magnitudes from -14 to -18, although they are all faint dwarfs, qualitatively similar to the hosts of SLSN Ic Lunnan et al. (2014); Leloudas et al. (2015); Chen et al. (2015).

We used both the MAGPHYS (da Cunha et al. 2008) and LEPHARE (Krühler et al. 2011) stellar population model programs to estimate the stellar mass from the observed optical photometric points. The program employs a library of stellar evolution and population synthesis models from Bruzual & Charlot (2003) and fits the luminosity of the host stellar population. The details about the fitting and the parameter extraction are discussed in Krühler et al. (2011) and Schulze et al. (in prep). We then retrieved a median stellar mass of $2.8^{+3.2}_{-1.6} \times 10^9$ M$_\odot$ and $4.8^{+2.0}_{-1.6} \times 10^7$ M$_\odot$ for SN 2013hx and PS15br, respectively. This allowed us to estimate the specific SFR

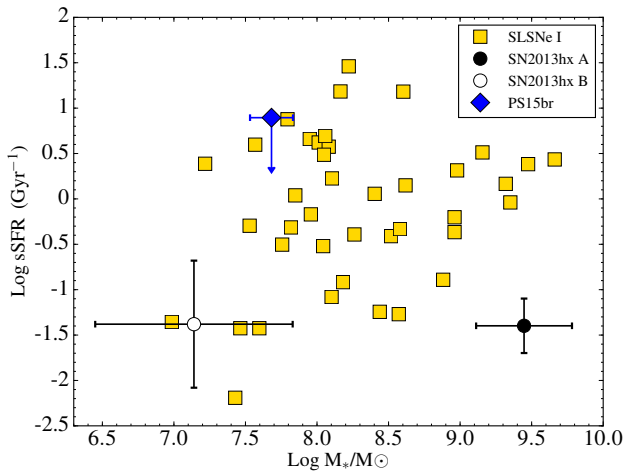

FIG. 16.— sSFR versus stellar mass of SN 2013hx (black dot) and PS15br (blue diamond) compared to those of SLSNe I (gold square; data from Lunnan et al. 2014; Chen et al. 2015; Leloudas et al. 2015). We note that the sSFR of PS15br is only an upper limit due to the upper limit of the SFR, see text.

(sSFR) for both our hosts, which are 0.004 Gyr^{-1} for SN 2013hx and 7.85 Gyr^{-1} for PS15br. As highlighted in Fig. 16, the galaxies are broadly similar to those of the SLSN I or Ic as quantified in Lunnan et al. (2014); Chen et al. (2015); Leloudas et al. (2015). They are low mass, and have relatively high specific star formation rates. We do not have metallicity measurements, but it seems safe to assume that their low mass and faint magnitudes imply a similarly low metallicity as have been measured for SLSN I when the relevant emission lines are detected Lunnan et al. (2014); Chen et al. (2013); Leloudas et al. (2015). However, the measurement for SN 2013hx should be taken with some caution due to the contamination with the SN flux and and a more precise measurement should be retrieved with a spectrum without any residual SN flux.

9. CONCLUSION

We have presented extensive photometric and spectroscopic coverage of two SLSNe II ($-20 > M_g > -22$). For one of them, SN 2013hx, we present a light curve up to 260 days, showing a well constrained rise time and a light curve evolution after 180d indicating a slow decline of the luminosity due to late interaction as shown by bright type II or IIL SNe.

SN 2013hx has $M_g = -21.7$ mag and $L_{bolometric} \approx 2.75 \times 10^{44}$ erg s^{-1} at peak, while PS15br shows $M_g \sim -20.2$ mag and $L_{bolometric} \approx 4.15 \times 10^{43}$ erg s^{-1} at maximum light. The former has a post peak light curve decline similar to that of SN 2008es and normal type IIL, whereas PS15br shows an initial decline comparable to that of SN 2013hx and a second, slower decline similar to those shown by transitional type IIn/IIL events at normal luminosity.

For PS15br we also obtained an epoch of broadband polarimetry at 6 days after maximum. After correcting for the ISP and the polarisation bias, we retrieved a polarised value of $P = 0.94 \pm 0.17\%$. However, this value strongly depends on the assumed ISP and hence no conclusive evidence on the source of the polarisation associated with PS15br can de derived.

SLSNe II show a spectroscopic evolution dominated by Balmer, He, Ca, Fe and other metal lines and an emission feature at early times at ∼4600 Å similar to that shown by SN 2008es. We identify this as He II λ4686 or C III/N III. SN 2013hx shows a late interaction (phase>140d) due to an asymmetric, clumpy CSM that dominates the late light curve behaviour. Moreover, regardless of the peak luminosity, their spectroscopic and temperature evolution resembles those of type IIL SNe with a delay of 15-20 days. This suggest as the transients are linked to type II SNe in a similar fashion as the SLSNe Ic are linked to type Ic SNe.

We also applied two semi-analytical codes to fit the light curves of our two objects and SN 2008es. The first based on the interaction between the ejecta and a dense uniform shell of H-rich material, while the second based on a diffusion model with energy input from a spinning down magnetar. We were able to reproduce the available bolometric light curve with $2.1 \lesssim M_{CSM}(M_\odot) \lesssim 2.8$ and $9.5 \lesssim M_{ej}(M_\odot) \lesssim 13.0$. While the late time light curve exhibited by SN 2013hx and driven by interaction can be fitted with a wind of 2.6 $M_\odot$ or a dense shell of 4.7 $M_\odot$. All light curves are also reproduced with feasible physical values for a magnetar including the data at 140-180 days of SN 2013hx, when the luminosity of our best fit model is lower than the data, which are already due to the aforementioned late interaction. To fit them we require $0.9 \lesssim B_{14} \lesssim 1.6$, $2.2 \lesssim P_{ms} \lesssim 6.4$ consistent with B of known galactic magnetars ($B_{14} \sim 1-10$) and with physically plausible periods ($P_{ms} > 1$). We derived energies of $0.4 \lesssim E^{mag}(10^{51}\ \mathrm{erg}) \lesssim 5.2$ and ejected masses of $1.9 \lesssim M_{ej}(M_\odot) \lesssim 6.9$. Both scenarios have their weaknesses. The high ejecta masses retrieved by the interaction model and the spectroscopic similarities to bright, linear type II regardless of the peak luminosity, would tend to disfavour of the interaction scenario. On the other hand, these characteristics can be better explained by the magnetar scenario.

Although the overall observables would favour the magnetar engine, the interaction shown at late phase by SN 2013hx does not allow a firm conclusion and suggests as interaction could play a role in the evolution of superluminous type II SNe. Despite our extensive data sets and analysis of this first sample of SLSNe II, open questions remain

- Do SLSNe II with interaction-free light curves exist? What should be their luminosity and what are the line profiles expected in a truly nebular spectrum?

- What is the role of metallicity in the progenitor stars evolution that will produce a H-rich SLSNe? It appears that they are all associated with faint dwarf galaxies and possibly low metallicity progenitors as those of SLSNe I.

- Can the geometry of the explosion play a role in the observables and/or shed light on the powering mechanism or their light curves?

As for the case of SLSNe I, to address these topics, high quality data and their modelling at early phase or

in an interaction-free nebular phase are needed to determine the ejecta masses, composition and the mass of ^{56}Co contributing to the luminosity. This seems the most likely way to make progress.

Pan-STARRS is supported by the University of Hawaii and the National Aeronautics and Space Administration's Planetary Defense Office under Grant No. NNX14AM74G. The Pan-STARRS1 Sky Surveys have been made possible through contributions by the Institute for Astronomy, the University of Hawaii, the Pan-STARRS Project Office, the Max Planck Society and its participating institutes, the Max Planck Institute for Astronomy, Heidelberg and the Max Planck Institute for Extraterrestrial Physics, Garching, The Johns Hopkins University, Durham University, the University of Edinburgh, the Queen's University Belfast, the Harvard-Smithsonian Center for Astrophysics, the Las Cumbres Observatory Global Telescope Network Incorporated, the National Central University of Taiwan, the Space Telescope Science Institute, and the National Aeronautics and Space Administration under Grant No. NNX08AR22G issued through the Planetary Science Division of the NASA Science Mission Directorate, the National Science Foundation Grant No. AST-1238877, the University of Maryland, Eotvos Lorand University (ELTE), and the Los Alamos National Laboratory. This work is based (in part) on observations collected at the European Organisation for Astronomical Research in the Southern Hemisphere, Chile as part of PESSTO, (the Public ESO Spectroscopic Survey for Transient Objects Survey) ESO programs188.D-3003, 191.D-0935. Some of the data presented herein were obtained at the Palomar Observatory, California Institute of Technology. The Liverpool Telescope is operated on the island of La Palma by Liverpool John Moores University in the Spanish Observatorio del Roque de los Muchachos of the Instituto de Astrofisica de Canarias with financial support from the UK Science and Technology Facilities Council. SJS acknowledges funding from the European Research Council under the European Union's Seventh Framework Programme (FP7/2007-2013)/ERC Grant agreement n^{o} [291222] and STFC grants ST/I001123/1 and ST/L000709/1. EEEG acknowledges support for this work by the Deutsche Forschungsgemeinschaft through the TransRegio project TRR33 'The Dark Universe'. SB is partially supported by the PRIN-INAF 2014 project Transient Universe: unveiling new types of stellar explosions with PESSTO. KM acknowledges support from the STFC through an Ernest Rutherford Fellowship. SP and RC acknowledge support from EU/FP7-ERC grant no [615929]. SS acknowledges support from CONICYT-Chile FONDECYT 3140534, Basal-CATA PFB-06/2007, and Project IC120009 "Millennium Institute of Astrophysics (MAS)" of Iniciativa Científica Milenio del Ministerio de Economía, Fomento y Turismo. This work was partly supported by the European Union FP7 programme through ERC grant number 320360. Part of this research was conducted by the Australian Research Council Centre of Excellence for All-sky Astrophysics (CAASTRO), through project number CE110001020

REFERENCES

Agnoletto, I., Benetti, S., Cappellaro, E., et al. 2009, ApJ, 691, 1348
Alam, S., Albareti, F. D., Allende Prieto, C., et al. 2015, ApJS, 219, 12
Alard, C. 2000, A&AS, 144, 363
Anderson, J. P., Dessart, L., Gutierrez, C. P., et al. 2014, MNRAS, 441, 671
Anderson, J. P., González-Gaitán, S., Hamuy, M., et al. 2014, ApJ, 786, 67
Andrews, J. E., Gallagher, J. S., Clayton, G. C., et al. 2010, ApJ, 715, 541
Angus, C. R., Levan, A. J., Perley, D. A., et al. 2016, MNRAS, 458, 84
Arcavi, I., Wolf, W. M., Howell, D. A., et al. 2016, ApJ, 819, 35
Baltay C., et al., 2007, PASP, 119, 1278
Baltay C., et al., 2013, PASP, 125, 683
Barbon R., Ciatti F., Rosino L., 1982, A&A, 116, 35
Barbon R., Ciatti F., Rosino L., Ortolani S., Rafanelli P., 1982, A&A, 116, 43
Barkat, Z., Rakavy, G., & Sack, N. 1967, Physical Review Letters, 18, 379
Benetti S., et al., 2014, MNRAS, 441, 289
Benetti, S., Chugai, N. N., Utrobin, V. P., et al. 2016, MNRAS, 456, 3296
Bessell M., Bloxham G., Schmidt B., Keller S., Tisserand P., Francis P., 2011, PASP, 123, 789
Botticella M. T., et al., 2010, ApJ, 717, L52
Blanton M. R., Roweis S., 2007, AJ, 133, 734
Blinnikov, S. I., & Bartunov, O. S. 1993, A&A, 273, 106
Brown, T. M., Baliber, N., Bianco, F. B., et al. 2013, PASP, 125, 1031
Bruzual, G., & Charlot, S. 2003, MNRAS, 344, 1000
Campbell H., et al., 2014, ATel, 5912, 1
Cappellaro E., Danziger I. J., Turatto M., 1995, MNRAS, 277, 106
Chatzopoulos, E., Wheeler, J. C., & Vinko, J. 2012, ApJ, 746, 121
Chatzopoulos, E., Wheeler, J. C., Vinko, J., Horvath, Z. L., & Nagy, A. 2013, ApJ, 773, 76
Chen, T.-W., Smartt, S. J., Jerkstrand, A., et al. 2015, MNRAS, 452, 1567
Chen, T.-W., Smartt, S. J., Bresolin, F., et al. 2013, ApJ, 763, L28
Chevalier, R. A., & Irwin, C. M. 2011, ApJ, 729, L6
Childress, M. J., Vogt, F. P. A., Nielsen, J., & Sharp, R. G. 2014, Ap&SS, 349, 617
Chomiuk, L., Chornock, R., Soderberg, A. M., et al. 2011, ApJ, 743, 114
Chugai, N. N. 1985, Soviet Astronomy Letters, 11, 148
da Cunha, E., Charlot, S., & Elbaz, D. 2008, MNRAS, 388, 1595
Dahlen, T., Strolger, L.-G., Riess, A. G., et al. 2012, ApJ, 757, 70
Dessart, L., & Hillier, D. J. 2005, A&A, 437, 667
Dessart, L., Hillier, D. J., Waldman, R., Livne, E., & Blondin, S. 2012, MNRAS, 426, L76
Dexter, J., & Kasen, D. 2013, ApJ, 772, 30
Dopita, M., Rhee, J., Farage, C., et al. 2010, Ap&SS, 327, 245
Drake, A. J., Djorgovski, S. G., Mahabal, A., et al. 2009, ApJ, 696, 870
Elmhamdi A., et al., 2003, MNRAS, 338, 939
Fesen R. A., et al., 1999, AJ, 117, 725
Filippenko A. V., 1997, ARA&A, 35, 309
Fraley, G. S. 1968, Ap&SS, 2, 96
Fraser, M., Smith, M., Firth, R., et al. 2015, The Astronomer's Telegram, 7209, 1
Freudling W., Romaniello M., Bramich D. M., Ballester P., Forchi V., García-Dabló C. E., Moehler S., Neeser M. J., 2013, A&A, 559, A96
Gal-Yam A., et al., 2009, Natur, 462, 624
Gal-Yam A., 2012, Sci, 337, 927
Gall E. E. E., et al., 2015, arXiv, arXiv:1502.06034
Gezari S., et al., 2009, ApJ, 690, 1313
Gutiérrez, C. P., Anderson, J. P., Hamuy, M., et al. 2014, ApJ, 786, L15

Hoflich, P. 1991, A&A, 246, 481
Hogg D. W., Baldry I. K., Blanton M. R., Eisenstein D. J., 2002, astro, arXiv:astro-ph/0210394
Huber M., et al., 2015, ATel, 7153, 1
Inserra C., et al., 2011, MNRAS, 417, 261
Inserra C., et al., 2012, MNRAS, 422, 1122
Inserra C., Baron E., Turatto M., 2012, MNRAS, 422, 1178
Inserra C., et al., 2013, A&A, 555, A142
Inserra C., et al., 2013, ApJ, 770, 128
Inserra C., et al., 2014, MNRAS, 437, L51
Inserra C., Smartt S. J., 2014, ApJ, 796, 87
Inserra C., et al., 2015, ApJ, 799, L2
Inserra, C., Fraser, M., Smartt, S. J., et al. 2015, arXiv:1510.01109
Janka, H.-T. 2012, Annual Review of Nuclear and Particle Science, 62, 407
Kangas, T., Mattila, S., Kankare, E., et al. 2016, MNRAS, 456, 323
Kasen, D., & Bildsten, L. 2010, ApJ, 717, 245
Kasen, D., Woosley, S. E., & Heger, A. 2011, ApJ, 734, 102
Kim A., Goobar A., Perlmutter S., 1996, PASP, 108, 190
Keller S., Bessell M., Schmidt B., Francis P., 2007, ASPC, 364, 177
Kennicutt, R. C., Jr. 1998, ARA&A, 36, 189
Kozma, C., & Fransson, C. 1998, ApJ, 497, 431
Krühler, T., Greiner, J., Schady, P., et al. 2011, A&A, 534, A108
Lantz, B., Aldering, G., Antilogus, P., et al. 2004, Proc. SPIE, 5249, 146
Leloudas, G., Patat, F., Maund, J. R., et al. 2015, ApJ, 815, L10
Leloudas, G., Schulze, S., Krühler, T., et al. 2015, MNRAS, 449, 917
Lunnan, R., Chornock, R., Berger, E., et al. 2014, ApJ, 787, 138
Magnier, E. A., Schlafly, E., Finkbeiner, D., et al. 2013, ApJS, 205, 20
Maguire K., et al., 2010, MNRAS, 404, 981
Mazzali, P. A., Sullivan, M., Pian, E., Greiner, J., & Kann, D. A. 2016, MNRAS,
Miller A. A., et al., 2009, ApJ, 690, 1303
Moriya, T. J., Liu, Z.-W., Mackey, J., Chen, T.-W., & Langer, N. 2015, arXiv:1510.01621
Nicholl, M., Smartt, S. J., Jerkstrand, A., et al. 2013, Nature, 502, 346
Nicholl M., et al., 2014, MNRAS, 444, 2096
Nicholl, M., Smartt, S. J., Jerkstrand, A., et al. 2015, ApJ, 807, L18
Nicholl, M., Smartt, S. J., Jerkstrand, A., et al. 2015, arXiv:1503.03310
Ofek, E. O., Cameron, P. B., Kasliwal, M. M., et al. 2007, ApJ, 659, L13
Oke J. B., Sandage A., 1968, ApJ, 154, 21
Pastorello A., et al., 2008, MNRAS, 389, 113
Pastorello A., et al., 2010, ApJ, 724, L16
Pastorello A., et al., 2015, MNRAS, 449, 1921
Patat F., Barbon R., Cappellaro E., Turatto M., 1993, A&AS, 98, 443
Patat, F., Cappellaro, E., Danziger, J., et al. 2001, ApJ, 555, 900
Patat, F., & Romaniello, M. 2006, PASP, 118, 146
Pignata G., et al., 2004, MNRAS, 355, 178
Polshaw et al. 2015, A&A, submitted
Poole T. S., et al., 2008, MNRAS, 383, 627
Pozzo, M., Meikle, W. P. S., Fassia, A., et al. 2004, MNRAS, 352, 457
Quimby, R. M., Aldering, G., Wheeler, J. C., et al. 2007, ApJ, 668, L99
Quimby R. M., et al., 2011, Natur, 474, 487
Quimby, R. M., Yuan, F., Akerlof, C., & Wheeler, J. C. 2013, MNRAS, 431, 912
Scalzo R., Yuan F., Childress M., Tucker B., Schmidt B., 2013, ATel, 5480, 1
Scalzo R., et al., 2014, CBET, 3836, 1
Schlafly E. F., Finkbeiner D. P., 2011, ApJ, 737, 103
Schlafly, E. F., Finkbeiner, D. P., Jurić, M., et al. 2012, ApJ, 756, 158
Smartt, S. J. 2009, ARA&A, 47, 63
Smartt, S. J. 2015, PASA, 32, e016
Smartt, S. J., Valenti, S., Fraser, M., et al. 2015, A&A, 579, A40
Smartt, S. J., Chambers, K. C., Smith, K. W., et al. 2016, arXiv:1602.04156
Smith, N., Li, W., Foley, R. J., et al. 2007, ApJ, 666, 1116
Smith, N., Humphreys, R. M., Davidson, K., et al. 2001, AJ, 121, 1111
Smith, N., Mauerhan, J. C., Cenko, S. B., et al. 2015, MNRAS, 449, 1876
Smith, N., & McCray, R. 2007, ApJ, 671, L17
Smith, N., & Owocki, S. P. 2006, ApJ, 645, L45
Steele, I. A., Smith, R. J., Rees, P. C., et al. 2004, Proc. SPIE, 5489, 679
Stritzinger M., et al., 2002, AJ, 124, 2100
Tomasella L., et al., 2013, MNRAS, 434, 1636
Tonry J. L., et al., 2012, ApJ, 750, 99
Turatto, M., Suzuki, T., Mazzali, P. A., et al. 2000, ApJ, 534, L57
Udalski A., Szymański M. K., Szymański G., 2015, AcA, 65, 1
Umeda, H., & Nomoto, K. 2008, ApJ, 673, 1014
Uomoto, A., & Kirshner, R. P. 1986, ApJ, 308, 685
Valenti S., et al., 2014, MNRAS, 438, L101
Valenti S., et al., 2015, MNRAS, 448, 2608
Vreeswijk P. M., et al., 2014, ApJ, 797, 24
Wang, S. Q., Wang, L. J., Dai, Z. G., & Wu, X. F. 2015, ApJ, 799, 107
Woosley, S. E. 2010, ApJ, 719, L204
Woosley, S. E., Blinnikov, S., & Heger, A. 2007, Nature, 450, 390
Woosley, S. E., & Weaver, T. A. 1995, ApJS, 101, 181
Yan, L., Quimby, R., Ofek, E., et al. 2015, arXiv:1508.04420
Xu, Y., McCray, R., Oliva, E., & Randich, S. 1992, ApJ, 386, 181
Yaron, O., & Gal-Yam, A. 2012, PASP, 124, 668

APPENDIX

S3 PACKAGE

The S3 package is a python suite publicly available at `https://github.com/cinserra` and accepts fits, txt, dat and ascii files as input. It contains the following programs.

SNAKE

The SuperNova Algorithm for K-correction Evaluation (SNAKE) and its light version developed to handle multiple input files in a less interactive fashion (SNAKELOOP) allow to evaluate the K-correction from the observed passband (P) to the rest-frame, desired passband (R) according to the formula defined in Oke & Sandage (1968); Hogg et al. (2002); Blanton & Roweis (2007):

$$K_{\rm PR} = -2.5\,\log\left[\frac{1}{1+z}\times\frac{\int d\lambda_{\rm o}\,\lambda_{\rm o}\,L_{\lambda}(\lambda_{\rm o}/(1+z))\,P(\lambda_{\rm o})\int d\lambda_{\rm e}\,\lambda_{\rm e}\,g^{R}_{\lambda}(\lambda_{\rm e})\,R(\lambda_{\rm e})}{\int d\lambda_{\rm o}\,\lambda_{\rm o}\,g^{P}_{\lambda}(\lambda_{\rm o})\,P(\lambda_{\rm o})\int d\lambda_{\rm e}\,\lambda_{\rm e}\,L_{\lambda}(\lambda_{\rm e})R(\lambda_{\rm e})}\right]\,, \tag{A1}$$

where $\mathrm{P}(\lambda)$ and $\mathrm{R}(\lambda)$ are the filter response per unit photon, $\mathrm{g}^{\rm passband}_{\lambda}$ are the flux densities per unit wavelength for the standard source for P and R, $\lambda_{\rm o}$ refers to the observer frame and $\lambda_{\rm e}$ to the rest-frame. We note that the S3 package uses flux and not density flux, hence the zero points are also treated accordingly. GALEX FUV and NUV; UVOT *uvw2*, *uvm2*, *uvw1*; Johnson UBVRI; Sloan *ugriz*; 2MASS JHK and 4000 Å and 5200 Å passbands (created for the use of SLSNe as cosmological probes in Inserra & Smartt 2014) are recognised by the program and the cross K-correction - which is when the observed and rest-frame filter shapes are the most similar - is suggested. In the case that more than 50 Å of one of the two filters chosen are not covered by the observer frame or rest-frame spectrum, the program allows the user to combine the spectrum with the best black-body fit to the data. The output of the program is the K-correction ($K_{\rm PR}$) and it is related to the apparent and absolute magnitude as follows:

$$\mathrm{M_R} = \mathrm{m_P} - (5\log \mathrm{D_L} + 25) - \mathrm{A_P} - K_{\rm PR}\,, \tag{A2}$$

in which $\mathrm{M_R}$ is the absolute magnitude in the rest-frame filter, $\mathrm{m_P}$ is the apparent magnitude in the observed filter, $\mathrm{D_L}$ is the distance luminosity of the source, $\mathrm{A_P}$ is the foreground reddening extinction toward the source in the observed band. Assuming as a first approximation that the terms are uncorrelated and evaluating the single term errors as their variance, the overall error on the K-correction is a root mean square:

$$\sigma_K = \sqrt{\frac{\sigma_z^2 + \sigma^2_{\mathrm{ZP}_{\lambda_{\rm o}}} + \sigma^2_{\mathrm{ZP}_{\lambda_{\rm e}}} + \sigma^2_{\rm BB}}{\mathrm{N}}}, \tag{A3}$$

where σ_z is the error on the redshift, which is set by default to be ± 0.005 and can be changed by the user; $\sigma_{ZP_{\lambda}}$ are the errors on the zero points for the observed (o) and rest-frame (e) filters evaluated from the average of all the differences between the zero points of the standard passbands (in the Vega and AB system) and those of the filters used by the telescopes listed in SNAP (cfr. Section A.2); $\sigma_{\rm BB}$ is the error on the assumption that a blackbody can be used to measure the wavelength uncovered by the spectrum for the filter chosen; N is the number of errors considered. Other two errors - related to the spectra template used in the case a spectrum of the object for the same, or very close in time, epoch of the photometry iare not available - should be considered, but the program does not handle that since they are highly dependent to the nature and the evolutionary phase of the object for which the K-correction is needed.

In order to test the program reliability we compared our results with those published by Kim, Goobar, & Perlmutter (1996) finding similar values. A previous, beta version, based on IRAF and STDAS was used to calculate K-corrections in Inserra & Smartt (2014); Inserra et al. (2015a), while this version has been used by Gall et al. (2015) and Polshaw et al. (2015). Furthermore, the program can also evaluate the K-correction when reddening is also applied and hence directly evaluate the term $-(\mathrm{A_P} + K_{\rm PR})$ of equation A2. However, this is not the correct way and the additional errors related to the assumed reddening and reddening law are not accounted for.

SNAP

The SuperNova Algorithm for P-correction (SNAP) evaluate a P-correction given by:

$$\mathrm{P}_{\lambda} = \mathrm{F}_{\lambda} \times \mathrm{QE}_{\lambda} \tag{A4}$$

where F_{λ} is the filter transmission function and QE_{λ} is the quantum efficiency of the detector. In contrast with the S-correction, the program does not take in account the lens throughput since, despite the use of a few materials, they are relatively flat across the optical range. However, this might cause some problems at wavelengths bluer than 3400 Å, i.e. affecting the U and *u* passbands. The atmospheric transmission profile is also ignored since SN magnitudes are usually evaluated through sequence stars calibrated with Sloan stars (and hence such correction is already taken in account at this level) or with Landolt stars and subsequent use of programs that apply such correction. We tested a

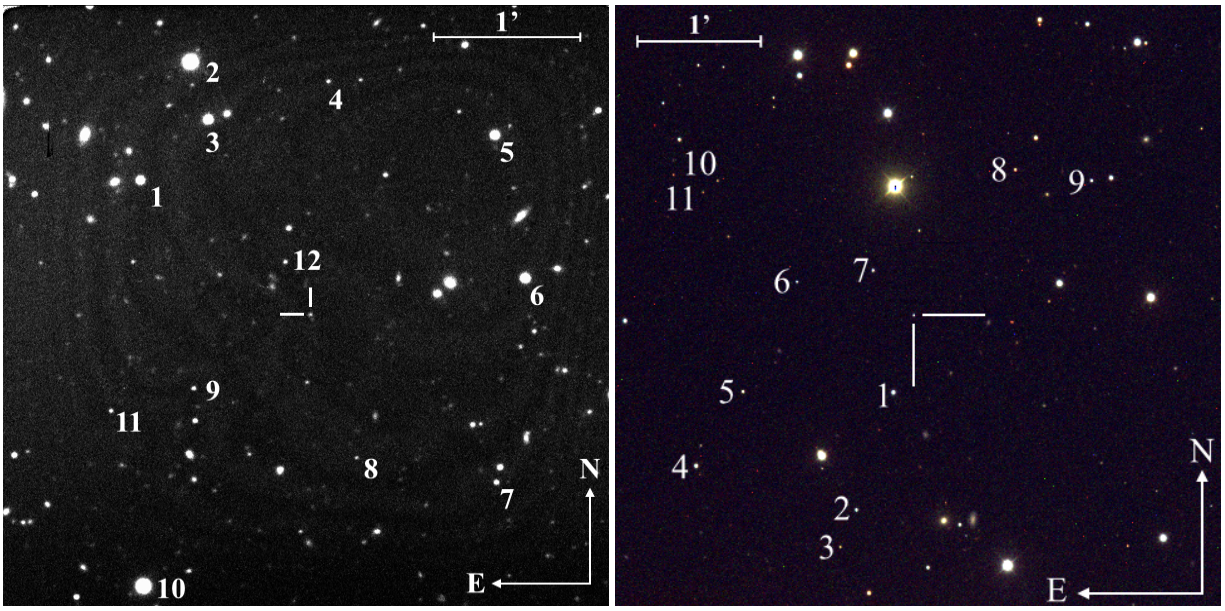

FIG. 17.— Left: NTT+EFOSC2+r image of SN 2013hx. The SN position is indicated with cross white marks. The sequence of stars in the field used to calibrate the optical and NIR magnitudes of SN 2013hx is indicated. Right: LT+IO+$g/r/i$ image of PS15br (cross white marks). The sequence of stars in the field used to calibrate the optical and NIR magnitudes of PS15br is indicated

few mirror reflectivity functions and found small dissimilarities between them, quantifiable in magnitudes differences smaller or comparable with the usual photometric errors; hence we decide to not include such additional term. Then the P_λ allows to correct the apparent magnitude of a given telescope to that of the standard passband system as follows:

$$m_P = m_F - P_\lambda, \tag{A5}$$

where m_P is the apparent magnitude with the standard passbands (Johnson UBVRI or Sloan *ugriz*) and m_F is the one measured with photometry at a given telescope. As SNAKE also SNAP evaluate the errors of the P-correction in the same way of equation A3 but without the redshift term and with the rest-frame filter considered as the error on the zero point in flux of the standard passband.

We retrieved the information needed for the P-correction for the New technology Telescope (NTT; ESO website), La Silla-Quest (LSQ; Baltay et al. 2007, and D. Rabinowitz private communication), SkyMapper (SMT; Bessell et al. 2011, M. Renault and R. Scalzo private communications), the Liverpool Telescope (LT; LT website), the Las Cumbres Observatory Global Network (LCOGT; S. Valenti private communication), the Optical Gravitational Lensing Experiment IV (OGLE-IV; Udalski, Szymański, & Szymański 2015, and L. Wyrzykowski private communication), the North Optical Telescope (NOT; NOT website), the Pan-STARSS1 survey (PS1; Tonry et al. 2012, and K. W. Smith private communications), the Telescopio Nazionale Galileo (TNG, TNG website), the Copernico Telescope at Cima Ekar in Asiago (EKAR, S. Benetti private communication).

SMS

The Synthetic Magnitudes from Spectra (SMS) program is just a python version of the STSDAS/HST IRAF tool calcphot. It evaluates the flux in a given passband and converts it in magnitudes (AB or Vega system) for the same filter list used by SNAKE. As SNAKE, it evaluates the errors in the same fashion of SNAKE but without the terms about the redshift and the rest-frame filter

TABLES

SEQUENCE STARS

TABLE 6
$UBVgriJHK$ MAGNITUDES OF SN 2013HX AND ASSIGNED ERRORS IN BRACKETS.

Date dd/mm/yy	MJD	Phase* (days)	U	B	V	g	r	i	Inst.
01/10/13	56566.61	-104.32	-	-	-	>20.86	>20.68	-	SMT
08/10/13	56573.58	-98.16	-	-	-	-	>20.71	-	SMT
19/10/13	56584.62	-88.39	-	-	-	>18.97	>19.24	-	SMT
28/10/13	56593.63	-80.41	-	-	-	>19.89	>19.65	-	SMT
01/11/13	56597.64	-76.87	-	-	-	>20.19	>19.98	-	SMT
06/11/13	56602.60	-72.48	-	-	-	>20.24	>20.02	-	SMT
10/11/13	56606.64	-68.90	-	-	-	>19.63	>19.64	-	SMT
15/11/13	56611.65	-64.47	-	-	-	>19.20	-	-	SMT
20/11/13	56616.62	-60.07	-	-	-	>18.59	>18.68	-	SMT
25/11/13	56621.60	-55.66	-	-	-	>20.03	>19.95	-	SMT
30/11/13	56626.58	-51.26	-	-	-	>19.94	>19.91	-	SMT
01/12/13	56627.55	-50.40	-	-	-	>20.30	>19.99	-	SMT
06/12/13	56632.55	-45.97	-	-	-	-	>20.28	-	SMT
27/12/13	56653.51	-27.42	-	-	-	17.86 (0.04)	18.14 (0.06)	-	SMT
31/12/13	56657.55	-23.85	-	-	-	17.50 (0.06)	17.83 (0.08)	-	SMT
04/01/14	56661.48	-20.37	-	-	-	17.33 (0.02)	17.61 (0.06)	-	SMT
04/01/14	56661.49	-20.36	-	-	-	17.32 (0.02)	17.62 (0.06)	-	SMT
05/01/14	56662.50	-19.47	-	-	-	17.27 (0.04)	17.52 (0.05)	-	SMT
07/01/14	56664.49	-17.71	-	-	-	17.09 (0.26)	17.47 (0.08)	-	SMT
07/01/14	56664.50	-17.70	-	-	-	17.20 (0.05)	17.43 (0.08)	-	SMT
25/01/14	56682.47	-1.80	-	-	-	16.88 (0.04)	17.07 (0.08)	-	SMT
26/01/14	56683.51	-0.88	-	-	-	16.89 (0.03)	17.09 (0.08)	-	SMT
26/01/14	56683.52	-0.87	-	-	-	16.88 (0.03)	17.06 (0.09)	-	SMT
27/01/14	56684.50	0.00	-	-	-	16.86 (0.27)	17.12 (0.13)	-	SMT
28/01/14	56685.49	0.88	-	-	-	16.89 (0.05)	17.12 (0.11)	-	SMT
29/01/14	56686.48	1.75	-	-	-	16.94 (0.04)	17.06 (0.10)	-	SMT
29/01/14	56686.49	1.76	-	-	-	16.95 (0.05)	17.13 (0.11)	-	SMT
30/01/14	56687.48	2.64	-	-	-	16.95 (0.06)	17.09 (0.09)	-	SMT
31/01/14	56688.47	3.51	-	-	-	-	17.14 (0.11)	-	SMT
06/02/14	56694.49	8.84	-	-	-	17.06 (0.05)	17.16 (0.09)	-	SMT
19/02/14	56708.03	20.82	-	-	16.76 (0.02)	-	-	-	NTT
20/02/14	56709.02	21.70	-	-	16.83 (0.01)	-	-	-	NTT
21/02/14	56709.88	22.56	17.08 (0.09)	17.67 (0.09)	16.89 (0.12)	-	-	-	SWIFT
21/02/14	56710.02	22.58	-	-	16.86 (0.02)	-	-	-	NTT
21/02/14	56711.02	23.47	-	-	16.87 (0.02)	-	-	-	NTT
24/02/14	56712.82	25.17	17.35 (0.08)	17.74 (0.10)	17.04 (0.19)	-	-	-	SWIFT
27/02/14	56715.36	27.43	17.48 (0.08)	17.91 (0.10)	17.21 (0.31)	-	-	-	SWIFT
28/02/14	56717.04	28.80	-	-	17.06 (0.02)	-	-	-	NTT
03/03/14	56719.16	30.81	17.73 (0.08)	17.78 (0.10)	17.15 (0.14)	-	-	-	SWIFT
05/03/14	56721.17	32.59	17.74 (0.09)	17.92 (0.10)	17.22 (0.14)	-	-	-	SWIFT
08/03/14	56724.56	35.61	17.96 (0.09)	18.07 (0.10)	17.29 (0.12)	-	-	-	SWIFT
08/03/14	56725.02	35.86	-	-	17.28 (0.02)	-	-	-	NTT
09/03/14	56726.02	36.74	-	-	17.40 (0.02)	-	-	-	NTT
10/03/14	56727.02	37.62	-	-	17.52 (0.02)	-	-	-	NTT
06/07/14	56844.40	141.50	-	22.30 (0.15)	21.80 (0.10)	22.32 (0.10)	21.80 (0.10)	20.70 (0.10)	LCOGT
10/07/14	56848.40	145.04	-	22.48 (0.15)	22.05 (0.10)	22.49 (0.10)	21.88 (0.10)	20.83 (0.10)	LCOGT
13/07/14	56851.72	147.98	-	-	-	-	>21.50	-	LCOGT
31/07/14	56869.68	163.88	-	-	-	>21.29	>20.94	-	SMT
15/08/14	56885.23	177.64	-	-	-	-	21.74 (0.09)	-	NTT
25/08/14	56895.17	186.43	-	-	-	-	21.87† (0.06)	21.50 (0.05)	NTT
21/09/14	56922.10	210.27	-	-	23.26 (0.19)	-	22.34† (0.06)	-	NTT
23/09/14	56924.15	212.08	-	-	-	23.72 (0.10)	22.54 (0.14)	21.80 (0.09)	NTT
21/10/14	56952.15	236.86	-	-	-	24.75 (0.17)	23.23 (0.24)	22.35 (0.14)	NTT
22/12/14	56975.11	257.18	-	-	-	24.96 (0.26)	23.68 (0.29)	22.80 (0.19)	NTT
18/02/15	57072.04	344.48	-	-	-	-	-	>24.00	NTT
Host A									
20/01/15	57043.09	318.75	-	-	-	-	23.26 (0.16)	-	NTT
10/12/15	57367.12	606.77	-	-	-	24.43 (0.16)	23.20 (0.16)	21.82 (0.16)	NTT
Host B									
01/02/16	57420.08	653.85	-	-	-	24.71 (0.38)	24.55 (0.35)	23.54 (0.32)	Mag

Date dd/mm/yy	MJD	Phase* (days)	J	H	K	Telescope
23/11/14	56985.12	266.03	22.21 (0.18)	>22.50	21.48 (0.12)	NTT
20/12/14	57012.10	289.91	-	-	22.10 (0.42)	NTT
29/12/14	57021.02	297.90	-	-	>22.18	NTT
Host A						
17/12/15	57374.12	613.00	>23.10	>23.00	> 23.20	NTT

* Phase with respect to the r-band maximum.

TABLE 7
griz MAGNITUDES OF PS15BR AND ASSIGNED ERRORS IN BRACKETS.

Date dd/mm/yy	MJD	Phase* (days)	g	r	i	z	Inst.
16/01/15	57038.41	-46.15	-	> 20.6	-	-	CSS
16/02/15	57069.43	-17.99	-	18.95† (0.07)	-	-	PSST
17/02/15	57070.43	-16.99	-	18.86† (0.07)	-	-	PSST
26/02/15	57079.48	-8.87	-	18.33 (0.07)	-	-	CSS
10/03/15	57091.52	2.06	-	18.24 (0.07)	-	-	CSS
11/03/15	57093.01	3.41	18.16 (0.01)	18.25 (0.01)	18.24 (0.01)	18.40 (0.02)	LT
14/03/15	57095.94	6.07	18.17 (0.01)	18.21 (0.01)	18.24 (0.02)	18.40 (0.03)	LT
19/03/15	57100.84	10.52	18.34 (0.07)	18.25 (0.07)	18.32 (0.07)	-	LCOGT
19/03/15	57100.91	10.59	18.31 (0.07)	18.29 (0.10)	18.33 (0.07)	-	LCOGT
21/03/15	57102.52	12.05	-	18.36 (0.07)	-	-	CSS
23/03/15	57104.57	13.91	18.45 (0.07)	18.38 (0.07)	18.37 (0.07)	-	LCOGT
24/03/15	57105.50	14.75	-	18.41† (0.07)	-	-	PSST
25/03/15	57106.51	15.67	-	18.44† (0.07)	-	-	PSST
27/03/15	57108.45	17.43	18.48 (0.07)	18.45 (0.08)	18.36 (0.07)	-	LCOGT
31/03/15	57112.90	21.47	18.57 (0.05)	18.40 (0.03)	18.36 (0.04)	18.45 (0.06)	LT
04/04/15	57117.03	25.22	18.58 (0.08)	18.42 (0.07)	18.40 (0.11)	-	LCOGT
07/04/15	57120.40	28.28	18.60 (0.09)	18.45 (0.08)	18.44 (0.11)	-	LCOGT
10/04/15	57121.52	29.29	-	18.52 (0.07)	-	-	CSS
10/04/15	57122.94	30.58	18.70 (0.01)	18.55 (0.02)	18.42 (0.01)	18.48 (0.06)	LT
11/04/15	57124.46	31.96	18.73 (0.08)	18.63 (0.08)	18.45 (0.11)	-	LCOGT
12/04/15	57124.94	32.40	18.77 (0.01)	18.61 (0.01)	18.46 (0.02)	18.50 (0.02)	LT
14/04/15	57126.94	34.21	18.78 (0.01)	18.61 (0.01)	18.48 (0.02)	18.48 (0.02)	LT
16/04/15	57128.44	35.58	-	18.66† (0.07)	-	-	PSST
16/04/15	57128.52	35.65	-	18.69 (0.07)	-	-	CSS
16/04/15	57128.99	36.07	18.96 (0.08)	-	-	-	LCOGT
17/04/15	57129.88	36.88	18.97 (0.09)	18.70 (0.08)	18.49 (0.11)	-	LCOGT
17/04/15	57129.93	36.93	18.95 (0.01)	18.66 (0.02)	18.50 (0.01)	18.49 (0.01)	LT
18/04/15	57130.42	37.37	-	18.67 (0.07)	-	-	PSST
20/04/15	57132.94	39.66	18.96 (0.02)	18.70 (0.01)	18.52 (0.01)	18.62 (0.02)	LT
22/04/15	57134.79	41.34	19.03 (0.09)	18.74 (0.08)	18.56 (0.11)		LCOGT
23/04/15	57135.95	42.39	19.06 (0.02)	18.74 (0.02)	18.48 (0.01)	18.53 (0.01)	LT
24/04/15	57136.52	42.91	-	18.71 (0.07)	-	-	CSS
25/04/15	57138.93	45.10	19.06 (0.02)	18.75 (0.02)	18.49 (0.02)	18.59 (0.02)	LT
26/04/15	57139.39	45.52	19.10 (0.10)	18.79 (0.07)	18.60 (0.08)	-	LCOGT
01/05/15	57144.29	49.96	19.21 (0.10)	18.79 (0.07)	18.58 (0.08)	-	LCOGT
02/05/15	57144.88	50.50	19.23 (0.06)	18.86 (0.07)	18.56 (0.03)	18.514 (0.03)	LT
04/05/15	57147.47	52.85	19.24 (0.10)	18.94 (0.07)	18.78 (0.08)	-	LCOGT
07/05/15	57149.52	54.71	-	18.92 (0.07)	-	-	CSS
08/05/15	57150.93	55.99	19.25 (0.02)	18.91 (0.01)	18.80 (0.03)	18.60 (0.02)	LT
10/05/15	57152.24	57.18	19.24 (0.10)	18.97 (0.07)	18.79 (0.08)	-	LCOGT
13/05/15	57155.52	60.16	-	18.97 (0.07)	-	-	CSS
14/05/15	57156.42	60.97	19.25 (0.10)	19.05 (0.07)	18.68 (0.08)	-	LCOGT
16/05/15	57158.86	63.19	19.23 (0.10)	19.05 (0.04)	18.74 (0.04)	18.71 (0.02)	LT
20/05/15	57162.87	66.83	19.25 (0.10)	19.05 (0.05)	18.72 (0.03)	18.76 (0.05)	LT
22/05/15	57164.52	68.33	-	19.10 (0.07)	-	-	CSS
24/05/15	57166.91	70.50	19.45 (0.03)	19.16 (0.03)	18.80 (0.02)	18.82 (0.02)	LT
02/06/15	57175.31	78.12	19.57 (0.15)	19.28 (0.15)	18.91 (0.12)	-	LCOGT
03/06/15	57176.97	79.63	19.56 (0.08)	19.31 (0.05)	18.90 (0.04)	19.03 (0.06)	LT
11/06/15	57184.27	86.26	19.83 (0.10)	19.39 (0.20)	19.10 (0.12)	-	LCOGT
12/06/15	57185.00	86.92	-	19.37 (0.20)	-	-	CSS
20/06/15	57193.37	94.52	-	-	19.15 (0.20)	-	LCOGT
30/06/15	57203.28	103.51	20.10 (0.20)	19.43 (0.15)	19.18 (0.10)	-	LCOGT
02/07/15	57205.27	105.32	20.30 (0.30)	19.75 (0.20)	19.28 (0.20)	-	LCOGT
Host							
01/05/10 - 01/10/14			22.39 (0.11)	22.18 (0.12)	21.70 (0.09)	22.15 (0.11)	PS1

* Phase with respect to the r-band maximum.
† r in the AB magnitude system from w-band filter converted through SNAP.

TABLE 8
$UBVJHK$ MAGNITUDES OF PS15BR AND ASSIGNED ERRORS IN BRACKETS.

Date dd/mm/yy	MJD (days)	Phase*	U	B	V	Inst.
10/03/15	57092.07	2.56	-	-	18.00 (0.01)	NTT
11/03/15	57092.87	3.29	17.88 (0.10)	18.44 (0.10)	18.04 (0.13)	SWIFT
12/03/15	57094.23	4.52	-	-	17.95 (0.01)	NTT
13/03/15	57095.20	5.40	-	-	17.97 (0.02)	NTT
14/03/15	57095.96	6.09	17.95 (0.13)	18.48 (0.13)	18.05 (0.19)	SWIFT
19/03/15	57100.84	10.52	-	18.51 (0.10)	18.10 (0.07)	LCOGT
19/03/15	57100.91	10.58	-	18.63 (0.08)	18.15 (0.07)	LCOGT
20/03/15	57102.22	11.77	18.32 (0.11)	18.64 (0.12)	18.18 (0.21)	SWIFT
23/03/15	57104.57	13.91	-	18.67 (0.08)	18.21 (0.07)	LCOGT
23/03/15	57105.14	14.42	18.65 (0.15)	18.73 (0.19)	18.21 (0.21)	SWIFT
26/03/15	57107.93	16.96	18.80 (0.15)	18.83 (0.19)	18.30 (0.23)	SWIFT
27/03/15	57108.45	17.43	-	18.82 (0.08)	18.34 (0.07)	LCOGT
27/03/15	57109.30	18.20	-	-	18.35 (0.06)	NTT
28/03/15	57110.04	18.87	-	-	18.30 (0.01)	NTT
30/03/15	57112.15	20.79	19.02 (0.18)	19.01 (0.13)	18.38 (0.21)	SWIFT
04/04/15	57116.99	25.18	19.22 (0.18)	19.04 (0.18)	18.43 (0.21)	SWIFT
04/04/15	57117.03	25.22	-	19.05 (0.15)	18.44 (0.10)	LCOGT
07/04/15	57119.98	27.90	19.42 (0.18)	19.07 (0.18)	18.50 (0.21)	SWIFT
07/04/15	57120.40	28.28	-	19.08 (0.15)	18.49 (0.14)	LCOGT
11/04/15	57124.46	31.96	-	19.17 (0.11)	18.58 (0.09)	LCOGT
16/04/15	57128.99	36.07	-	19.19 (0.13)	18.76 (0.10)	LCOGT
17/04/15	57129.88	36.88	-	19.30 (0.11)	18.79 (0.11)	LCOGT
18/04/15	57130.81	37.73	-	19.45 (0.11)	18.80 (0.09)	LCOGT
22/04/15	57134.79	41.34	-	19.47 (0.20)	18.85 (0.11)	LCOGT
25/04/15	57138.13	44.37	-	-	18.84 (0.03)	NTT
26/04/15	57139.39	45.52	-	19.44 (0.12)	18.81 (0.10)	LCOGT
01/05/15	57144.29	49.96	-	19.43 (0.12)	18.84 (0.10)	LCOGT
04/05/15	57147.47	52.85	-	19.42 (0.12)	18.84 (0.10)	LCOGT
10/05/15	57152.24	57.18	-	19.59 (0.12)	18.86 (0.10)	LCOGT
14/05/15	57156.42	60.97	-	19.67 (0.20)	19.15 (0.10)	LCOGT
Date dd/mm/yy	MJD (days)	Phase*	J	H	K	Telescope
11/03/15	57093.22	3.60	17.796 (0.02)	17.475 (0.03)	17.274 (0.06)	NTT
16/04/15	57129.14	36.21	17.763 (0.01)	17.226 (0.01)	17.012 (0.02)	NTT

* Phase with respect to the r-band maximum.

TABLE 9
Swift+UVOT *uvw2uvm2uvw1* magnitudes of SN 2013hx and PS15br and assigned errors in brackets.

Date dd/mm/yy	MJD	Phase* (days)	*uvw2*	*uvm2*	*uvw1*
			SN 2013hx		
21/02/14	56709.88	22.56	17.67 .10	17.44 .08	17.17 .09
24/02/14	56712.82	25.17	17.87 .10	17.75 .08	17.46 .09
27/02/14	56715.36	27.43	18.10 .12	18.05 .16	17.63 .09
03/03/14	56719.16	30.81	18.49 .12	18.13 .10	18.01 .11
05/03/14	56721.17	32.59	18.58 .13	18.38 .11	18.07 .13
08/03/14	56724.56	35.61	18.85 .13	18.58 .11	18.34 .12
27/04/14	56774.90	80.35	-	>21.0	-
28/04/14	56775.03	80.47	-	-	>21.8
30/04/14	56777.36	82.54	>22.0	-	-
07/07/14	56845.79	143.37	>21.9	-	-
21/07/14	56859.07	155.17	-	-	>21.6
24/07/14	56862.46	158.19	-	>21.1	-
			PS15br		
11/03/15	57092.87	3.29	18.70 (0.11)	18.67 (0.17)	18.25 (0.11)
14/03/15	57095.96	6.09	19.01 (0.17)	18.87 (0.22)	18.50 (0.18)
20/03/15	57102.22	11.77	19.37 (0.14)	19.24 (0.19)	18.83 (0.15)
23/03/15	57105.14	14.42	19.57 (0.21)	19.44 (0.32)	18.85 (0.15)
26/03/15	57107.93	16.96	19.78 (0.18)	19.13 (0.19)	18.92 (0.16)
30/03/15	57112.15	20.79	20.06 (0.19)	19.77 (0.24)	19.29 (0.18)
04/04/15	57116.99	25.18	20.26 (0.30)	19.94 (0.26)	19.47 (0.24)
07/04/15	57119.98	27.90	20.39 (0.24)	20.03 (0.28)	19.62 (0.28)

* Phase with respect to the r-band maximum.

TABLE 10
Magnitudes in *BVgri* of the local sequence stars in the field of SN 2013hx.

Star	*B*	*V*	*g*	*r*	*i*
1	21.06 (0.09)	19.24 (0.05)	19.35 (0.03)	17.81 (0.03)	16.55 (0.02)
2	18.96 (0.06)	16.68 (0.02)	16.83 (0.02)	15.26 (0.03)	13.81 (0.02)
3	19.59 (0.07)	18.17 (0.03)	17.98 (0.02)	17.30 (0.02)	16.69 (0.02)
4	-	22.89 (0.09)	22.90 (0.08)	21.17 (0.08)	20.65 (0.05)
5	20.56 (0.08)	18.76 (0.05)	18.90 (0.04)	17.39 (0.05)	15.94 (0.02)
6	19.29 (0.07)	17.95 (0.06)	17.72 (0.03)	17.20 (0.03)	16.65 (0.03)
7	-	22.50 (0.09)	22.17 (0.06)	20.41 (0.05)	18.40 (0.04)
8	-	22.50 (0.08)	22.61 (0.09)	21.82 (0.08)	21.34 (0.06)
9	-	22.54 (0.08)	22.77 (0.09)	21.11 (0.07)	19.13 (0.04)
10	17.42 (0.05)	16.04 (0.02)	15.83 (0.02)	15.15 (0.02)	14.67 (0.03)
11	-	22.22 (0.08)	22.38 (0.08)	21.07 (0.07)	20.21 (0.05)
12	-	22.36 (0.08)	22.50 (0.09)	21.15 (0.07)	20.28 (0.05)

TABLE 11
Magnitudes in *BVgriz* of the local sequence stars in the field of PS15br.

Star	*B*	*V*	*g*	*r*	*i*	*z*
1	16.50 (0.02)	16.02 (0.02)	16.19 (0.01)	15.96 (0.01)	15.83 (0.02)	15.83 (0.01)
2	18.02 (0.02)	17.47 (0.02)	17.67 (0.01)	17.38 (0.01)	17.22 (0.01)	17.18 (0.01)
3	20.57 (0.05)	19.32 (0.03)	19.86 (0.02)	18.85 (0.01)	18.27 (0.01)	17.97 (0.01)
4	17.41 (0.02)	16.51 (0.02)	16.91 (0.01)	16.16 (0.01)	15.85 (0.01)	15.69 (0.01)
5	19.03 (0.03)	17.89 (0.02)	18.41 (0.01)	17.44 (0.01)	16.97 (0.01)	16.72 (0.01)
6	19.12 (0.03)	18.65 (0.03)	18.81 (0.02)	18.60 (0.01)	18.49 (0.01)	18.47 (0.01)
7	18.33 (0.03)	17.80 (0.02)	17.99 (0.01)	17.70 (0.01)	17.55 (0.01)	17.52 (0.01)
8	20.17 (0.05)	18.51 (0.03)	19.07 (0.02)	17.89 (0.01)	16.96 (0.01)	16.49 (0.01)
9	18.07 (0.02)	17.44 (0.02)	17.68 (0.01)	17.29 (0.01)	17.08 (0.01)	17.01 (0.01)
10	20.75 (0.05)	19.59 (0.05)	20.09 (0.02)	19.15 (0.01)	18.63 (0.01)	18.37 (0.01)
11	21.48 (0.06)	20.15 (0.05)	20.72 (0.03)	19.63 (0.02)	19.03 (0.02)	18.66 (0.01)

TABLE 12
Journal of spectroscopic observations.

Date dd/mm/yy	MJD	Phase* (days)	Range† (Å)	Resolution	Instrumental Configuration
SN 2013hx					
31/01/14	56688.43	3.49	3100–6900	1.5/2.5	ANU 2.3m+WiFeS+B300/R300
19/02/14	56708.03	20.82	3600–9300	18	NTT+EFOSC2+gm13
20/02/14	56709.02	21.70	3600–9300	18	NTT+EFOSC2+gm13
21/02/14	56710.02	22.58	6000–10000	16	NTT+EFOSC2+gm16
22/02/14	56711.02	23.47	3300–7500	13	NTT+EFOSC2+gm11
24/02/14	56712.44	24.84	3400–6900	1.5/2.5	ANU 2.3m+WiFeS+B300/R300
28/02/14	56717.04	28.80	3300–10000	13/16	NTT+EFOSC2+gm11/gm16
04/03/14	56720.42	31.93	3400-6900	1.5/2.5	ANU 2.3m+WiFeS+B300/R300
08/03/14	56725.03	35.87	6000–10000	16	NTT+EFOSC2+gm16
09/03/14	56726.06	36.78	3300–10000	13/16	NTT+EFOSC2+gm11/gm16
10/03/14	56727.02	37.62	3300–7500	13	NTT+EFOSC2+gm11
14/03/14	56730.39	40.79	3400–6900	1.5/2.5	ANU 2.3m+WiFeS+B300/R300
21/09/14	56922.10	210.27	6900–7700	18	NTT+EFOSC2+gm13
22/10/14	56953.07	237.67	4500–9300	11	VLT+FORS2+GRIS_300V
PS15br					
10/03/15	57092.07	2.56	3600–9300	18	NTT+EFOSC2+gm13
12/03/15	57093.56	3.91	4100–6900	1.5/2.5	ANU 2.3m+WiFeS+B300/R300
12/03/15	57094.23	4.52	3300–7500	13	NTT+EFOSC2+gm11
13/03/15	57095.20	5.40	6000–10000	16	NTT+EFOSC2+gm16
27/03/15	57109.30	18.20	3300–10000	18	NTT+EFOSC2+gm13
28/03/15	57100.05	18.88	3600–9300	18	NTT+EFOSC2+gm13
12/04/15	57125.06	32.51	3600–9300	18	NTT+EFOSC2+gm13
25/04/15	57138.13	44.37	3600–9300	18	NTT+EFOSC2+gm13
29/06/15	57202.13	102.47	3600–9300	4.3/5.8	UH 2.2m+SNIFS+B/R

* Phase with respect to the r-band maximum.
† Range with respect to the observed frame.